REPRESENTATION OF 3D PHENOMENA OF LAMINAR FLOW AND HEAT TRANSFER IN A HELICALLY COILED TUBE USING A 2D GEOMETRY

Nilo Henrique Meira Fortes, Artemio Plana-Fattori, Jorge Audrey Wilhelms Gut

REPRESENTATION OF 3D PHENOMENA OF LAMINAR FLOW AND HEAT TRANSFER IN A HELICALLY COILED TUBE USING A 2D GEOMETRY

Nilo Henrique Meira Fortes[1], Artemio Plana-Fattori[2], Jorge Andrey Wilhelms Gut[1,3,*]

[1] *Universidade de São Paulo, Escola Politécnica, Dept. of Chemical Engineering, 05508-000, São Paulo, Brazil*

[2] *Université Paris-Saclay, INRAE, AgroParisTech, UMR SayFood, 91120, Palaiseau, France*

[3] *Universidade de São Paulo, FoRC – Food Research Center, 05508-080, São Paulo, Brazil*

* Corresponding author. Tel.: +55-11-30912253.

E-mail address: jorgewgut@usp.br (J. A. W. Gut).

Abstract

The coiled tube geometry has different industrial applications whereby heating and cooling operations are required. In this work, a 2D semi-empirical model based on a straight tube is proposed to represent the 3D phenomena of flow and heat transfer in a coiled tube. The model considers a modified velocity profile based on residence time distribution (RTD) experiments and a heat transfer enhancement factor based on heating and cooling experiments. For testing and validating the model, experiments were performed using a Newtonian fluid (glycerin/water mixture) and a non-Newtonian fluid (carboxymethylcellulose CMC solution) at flow rates from 0.5 to 2.0 L/min in a coiled tube with 9 turns. The y-laminar RTD model was successfully adjusted to experimental E-curves and its parameter y was correlated with flow rate. Heating and cooling

experiments with the coil provided outlet temperatures at different conditions of flow rate and temperature. The model was adjusted to match the outlet temperatures, providing the heat transfer enhancement factor F, the second empirical parameter of the model. This factor was linearly correlated with Reynolds number in a log-log plot and showed a threshold for negligible enhancement (F = 1). The model was numerically solved the finite difference method after a mesh dependency study. Good outlet temperature predictions were obtained with computational time of about 1 min, which is much smaller than usual computational times for a 3D coil geometry, and model provides velocity and temperature fields useful for further simulation of non-isothermal laminar flow reactors, such as bacterial inactivation in thermal processing of liquid foods.

Keywords

Heat transfer enhancement; Heat exchanger; Laminar flow; Residence time distribution; Coiled tube; Dean vortices

NOMENCLATURE

$A(t)$	exit absorbance of tracer (-)
A_0	initial absorbance of tracer (-)
A_e	external surface area of the tube (m^2)
A_i	internal surface area of the tube (m^2)
$C(t)$	exit concentration of tracer ($kg.m^{-3}$)
C_0	initial concentration of tracer ($kg.m^{-3}$)
C_p	Specific heat capacity at constant pressure ($J.kg^{-1}.K^{-1}$)
d_c	coil diameter (m)
d_e	tube external diameter (m)

d_{eq}	equivalent diameter of the duct (m)
d_i	tube internal diameter (m)
D	Mass diffusivity ($m^2.s^{-1}$)
De	Dean number (-)
$E(t)$	exit age distribution function (s^{-1})
$E_{exp}(t)$	exit age distribution function of experimental data (s^{-1})
$E_{model}(t)$	exit age distribution function of the model (s^{-1})
$E_\theta(\theta)$	dimensionless exit age distribution function (-)
f	Theoretical friction factor for laminar flow in tube with smooth walls (-)
f_{eff}	Effective friction factor (-)
F	heat transfer enhancement factor (-)
h	convective heat transfer coefficient of the internal fluid ($W.m^{-2}.K^{-1}$)
h_e	convective heat transfer coefficient of the external fluid ($W.m^{-2}.K^{-1}$)
k	thermal conductivity ($W.m^{-1}.K^{-1}$)
k_{eff}	effective thermal conductivity ($W.m^{-1}.K^{-1}$)
k_s	thermal conductivity of the solid ($W.m^{-1}.K^{-1}$)
K	consistency coefficient ($Pa.s^n$)
l	characteristic length of the geometry (m)
L	calculated linear length of the tube (m)
m	parameter of the m-laminar model (-)
n	number of turns of the coil or flow behavior index (-)
Nu	Nusselt number (-)
p	coil pitch (m)
Pe	Peclet number (-)

Pr	Prandtl number (-)
q	heat transfer rate (W)
$\dot{q}_V$	volumetric thermal energy generation ($W.m^{-3}$)
Q	volumetric flow rate ($m^3.s^{-1}$)
r	radial dimension (m)
r_i	tube internal radius (m)
r_e	tube external radius (m)
r^*	dimensionless radius (-)
R^2	coefficient of determination (-)
Re	Reynolds number (-)
Re_{crit}	critical Reynolds number (-)
Re_g	generalized Reynolds number (-)
t_m	mean residence time (s)
T_b	bulk temperature (K)
T_i	initial temperature (K)
T_{in}	inlet temperature (K)
T_m	average temperature (K)
T_{out}	outlet temperature (K)
T_e	external temperature (K)
U	Overall heat transfer coefficient ($W.m^{-2}.K^{-1}$)
v_b	bulk velocity ($m.s^{-1}$)
v_{in}	inlet velocity ($m.s^{-1}$)
v_{max}	maximum velocity ($m.s^{-1}$)
v_z	axial component of velocity ($m.s^{-1}$)

$\vec{v}$	velocity vector (m.s^{-1})
v^*	dimensionless velocity (-)
V	internal volume of the tube (m^3)
V_A	active volume of the tube (m^3)
V_s	volume of the solid (m^3)
y	y-laminar model parameter (-)
z	axial dimension (m)

Greek letters

α	thermal diffusivity (m^{-2}.s^{-1}) or parameter of the sinusoidal model (-)
α_{eff}	effective thermal diffusivity (m^{-2}.s^{-1})
β	parameter of the exponential model (-)
δ	curvature ratio (-)
ε	Friction factor enhancement factor (-)
θ_0	dimensionless breakthrough time (-)
μ	dynamic viscosity (Pa.s)
μ_g	generalized viscosity (Pa.s)
ν	kinematic viscosity (m^2.s^{-1})
ξ	geometrical parameter of the duct (-)
φ	geometrical parameter of the duct (-)
ρ	density (kg.m^{-3})
τ	theoretical residence time (s)

1. INTRODUCTION

The coiled or helical tube geometry is widely used in processes that involve continuous flow chemical reactions and/or heat transfer because of its compact structure, enhanced mixing and passive heat transfer enhancement under laminar flow [1,2]. The centrifugal forces experienced by the fluid due to the coil curvature generate secondary flow structures called Dean cells, a pair of counter-rotating symmetrical vortices at the cross-section of the tube that moves fluid outward from the curvature center of the coil. This circulation of fluid promotes local mixing and increases heat transfer rate and chemical reaction yield [3].

The effects of the tube curvature on the flow can be characterized by the Dean number (De), a dimensionless group that relates the Reynolds number (Re) with the square root of the curvature ratio ($\delta = d_i/d_c$) according to Eq. (1) for tubes with small torsion (ratio between coil pitch and coil radius) [4]. The Reynolds number is the ratio of inertial forces to viscous forces, as defined in Eq. (2):

$$De = Re\sqrt{d_i/d_c} \tag{1}$$

$$Re = \frac{\rho\, d_i v_b}{\mu} \tag{2}$$

where d_i is the tube internal diameter, d_c is the coil or curve diameter, v_b is the bulk velocity, ρ is the average fluid density and μ is the average fluid viscosity [5,6].

The flow pattern inside a coiled tube is complex due to the secondary flow, especially in laminar flow with small Reynolds numbers [7]. The geometrical characteristics of the coil, particularly the curvature ratio and the pitch, influence the degree of fluid mixing. Also, Dean instabilities may arise above a threshold Dean number, which creates additional pairs of counter-rotating vortices at the outer wall of tube. This critical value is unique for each coil, since it depends on the coil curvature ratio (δ) and cross-section aspect ratio (ratio between height and width) [8].

The flow pattern inside tubes can be studied using the concept of residence time distribution (RTD), which is defined as the distribution of time that fluids spend inside a vessel. Usually, RTD is determined experimentally by injecting a tracer at the inlet and measuring its concentration at the outlet over time, $C(t)$. The exit age distribution function $E(t)$, or E-curve, is defined in Eq. (3a), while the mean residence time is defined in Eq. (3b) and the dimensionless E-curve in Eq. (3c), where $\theta = t/t_m$ is the dimensionless time. The E-curve is important to characterize flow pattern and dispersion inside vessels [9].

$$E(t) = \frac{C(t)}{\int_0^\infty C(t)\,\mathrm{d}t} \tag{3a}$$

$$t_m = \int_0^\infty t\,E(t)\,\mathrm{d}t \tag{3b}$$

$$E_\theta(\theta) = t_m\,E(t) \tag{3c}$$

The RTD in tubes with laminar flow is related to the dispersion caused by the mechanisms of convection (axial velocity profile) and molecular diffusion (in axial and radial directions), constituting the Taylor-Aris dispersion. The laminar velocity profile promotes a large spread in the E-curve, while the radial diffusion promotes mixing between layers, thus reducing this spread. The secondary flow that arises from the flow in curves and helical pipes also contributes to narrow the dispersion in the E-curve and to delay the first appearance of the tracer, because it promotes convective mixing in the cross section of the tube [9,10,11].

Florit et al. [11] studied the axial dispersion in coiled reactors with computational fluid dynamics (CFD) using the finite volume method in 3D simulations. Different geometrical parameters were considered, such as coil pitch, coil radius and tube length, while a single value of tube diameter was chosen. Transient CFD simulations were used

88 to evaluate the residence time distribution (RTD) in the coil, which was represented by
89 the axial dispersion model (ADM). RTD experiments were performed to determine the
90 dispersion number (parameter of the ADM) using a blue dye as tracer (pulse injection)
91 and water as fluid. The CFD results were in good agreement with experimental data and
92 a reduction was observed in the axial dispersion in the coiled tubes when compared to
93 flow in straight tubes.

94 Sharma et al. [12] studied mixing in coiled tubes and coiled flow inverters in
95 different flow regimes. RTD experiments were conducted by the colorimetric method,
96 using water as solvent and a red dye as tracer. The results were evaluated in terms of the
97 Peclet number, a dimensionless group that represents the ratio between advection and
98 mass diffusion (Eq. 4a) or thermal diffusion (Eq. 4b):

$$Pe = \frac{l\, v_b}{D} \tag{4a}$$

$$Pe = \frac{l\, v_b}{\alpha} \tag{4b}$$

99 where D is the mass diffusivity or diffusion coefficient, α is the thermal diffusivity and l
100 is the characteristic length of the geometry (diameter for circular tubes). Plots of Peclet
101 number versus Reynolds number indicated that: in laminar flow, the Dean vortices have
102 a strong influence in mixing; in the transition zone, the effect of the Dean vortices is
103 balanced by the increase in the axial dispersion induced by the velocity profile; in the
104 turbulent regime, the cross-sectional mixing dominates.

105 Different types of heat exchangers can be used for heating and cooling, depending
106 on the application. Plate heat exchangers are widely used in the food industry for low
107 viscosity fluids because of the compactness and ease of cleaning; however, pressure drop
108 is a limiting factor. Shell and tube heat exchangers are more versatile in terms of pressure
109 and temperature conditions [13,14]. For highly viscous fluids and small flow rates, coiled

or helical heat exchangers are a common choice due to compactness, enhanced heat transfer and lower pressure drop [15]. The coiled geometry can be used to construct different types of heat exchangers, such as coiled double-pipe heat exchangers, shell and helically coiled tube heat exchangers and helical coil heat exchangers. Kushwaha et al. [16] numerically studied heat transfer and fluid flow in a coiled double-pipe heat exchanger with a Newtonian and a non-Newtonian fluid; Reddy et al. [17] used CFD to study the improvement in heat transfer in a coiled double-pipe heat exchanger with different geometries for the inner tube; Bozzoli et al. [18] studied the local Nusselt number and showed that at the outside surface of the coil, it can be five times larger than that at the inside surface because of the secondary flow; and Wang et al. [19] studied the optimal design of a double-pipe heat exchanger based on the outward helically corrugated tube.

Examples of application of the shell and helically coiled tube heat exchangers can be found in recent literature. Maghrabie et al. [20] performed an experimental study with a shell and helically coiled tube heat exchanger considering different inclination angles; Raut et al. [21] numerically studied the effect of geometrical and operational parameters of a shell-and-tube heat exchanger in a process of paraffin melting; and Wang et al. [22] conducted an experimental and numerical study on the heat transfer and flow based on multi-objective optimization in a shell and helically coiled tube heat exchanger.

Helical coil heat exchangers have different applications. Lei and Bao [23] experimentally studied the laminar heat transfer at supercritical pressure in a helical coiled tube; Oliveira et al. [24] developed a model to calculate the pressure loss of Newtonian and non-Newtonian fluids in coiled tubes with experimental validation; and Xu et al. [25] developed a model based on the simulation code RELAP5 to study the thermo-hydraulic characteristics of helically coiled tubes.

A variety of tube configurations and accessories have been studied as additional methods to improve heat transfer in coiled tubes, e.g. flow inverter/reverser [26,27], helical tube with fins [28], tubes with corrugated wall [29,30], and twisted tapes/wired coils inside the tube [31,32].

Many of the studies on flow, heat transfer and dispersion in coiled tubes are conducted using CFD software because of the complex flow pattern generated by the secondary flow. Numerical simulations in such cases require an accurate modeling using refined 3D meshes with a large number of elements to adequately represent the mixing phenomenon [33]. Moreover, the use of accessories in tubes and/or different tube configurations further increases the model complexity and the computational cost (memory and time).

Simplified models that describe flow and heat transfer in coiled tubes are an alternative to complex 3D models, because simpler models require less computational time, which allows them to be implemented in optimization problems or in predictive control in the industry. An approach to study mixing in laminar flow in 3D and 2D models was proposed by Galaktionov et al. [34,35]. The method is known as mapping approach and consists of numerical simulations for the accurate tracking of fluid volumes in small intervals of time or space. The flow domain is subdivided into small subdomains (creating a mesh) and mixture is described in these subdomains with local averaged values, usually concentrations. Then, the flow is established as a sequence of discrete steps using the subdomains and then the concentration values are stored in a mapping matrix. This method requires knowledge of the velocity field and complex geometries may increase computational costs.

A semi-empirical approach to study flow and heat transfer in tubes was realized by Morais and Gut [36]. A 2D model was proposed for laminar flow in a straight tube

160 with enhanced radial heat transfer. The objective was to simulate heat transfer in systems
161 with enhanced mixing, such as coiled or corrugated tubes. A heat transfer enhancement
162 factor was defined in terms of a modified Peclet number. The results indicated that the
163 effective radial thermal diffusivity in a coiled tube (experimental) was up to six times
164 higher than the fluid property; however, the laminar flow velocity profile used in their
165 model did not adequately represent the residence time distribution (RTD) in the coiled
166 tube, which would compromise reaction yield calculations for a non-isothermal LFR
167 (Laminar Flow Reactor).

168 Dantas and Gut [37] applied this model to simulate the continuous-flow thermal
169 processing of a liquid food with associations of double-pipe heat exchangers for heating
170 and cooling. Enhanced radial heat and mass diffusions were considered for straight tube
171 laminar flow of the food product because of the high relative roughness of the tube.
172 Simulation results provided the time-temperature history of the product along the process
173 with the corresponding rates of inactivation of the target microorganism and of loss of
174 quality due to high temperature. It was possible to see how enhanced heat transfer or
175 enhanced diffusion in the radial direction can largely impact the process lethality or yield;
176 however, there was no experimental validation of the model.

177 Therefore, the objective of this study was to develop and to experimentally
178 validate a 2D semi-empirical model to represent laminar flow RTD and heat transfer in a
179 coiled tube. The original 3D problem was reduced to a 2D axisymmetric problem in a
180 straight tube geometry with the same linear length, but with enhanced heat transfer and
181 adjusted velocity profile. A velocity profile deriving from a RTD model obtained from
182 experiments was introduced to better represent the flow and dispersion in the coiled tube,
183 which is an important improvement over previous studies.

2. MATHEMATICAL MODELING

The flow and heat transfer in a coiled tube is inherently a 3D phenomenon. In order to build a 2D model, a straight tube with length L and internal diameter d_i was considered (Fig. 1); however, the shape of the velocity profile is going to be changed to match the real E-curve of the coiled tube and a heat transfer enhancement factor in the radial direction will be introduced to match the real heat transfer rate of the coiled tube. As further explained, since these two modifications rely on experimental data for parameter estimation, this 2D model is semi-empirical.

The model uses a cylindrical coordinate system with temperature varying with z and r, axial velocity varying with r, a fluid with inlet temperature T_{in}, inlet volumetric flow rate Q_{in} and a heat transfer rate $q(z)$ on the tube wall.

The length of the straight tube is equal to the linear length of the coiled tube (center line), which can be calculated with Eq. (5) [38]:

$$L = n\sqrt{p^2 + \pi(d_c + d_e)^2} \tag{5}$$

where n is the number of turns of the coil, p is the coil pitch, d_c is the coil diameter and d_e is the tube external diameter.

The heat transfer was evaluated using the energy conservation equation (Eq. 6) [5,39]:

$$\frac{\partial(T\rho C_p)}{\partial t} + \vec{v}\,\nabla(\rho C_p T) = \nabla(k\nabla T) + \dot{q}_V \tag{6}$$

where T is the temperature, ρ is the fluid density, C_p is the specific heat capacity, $\vec{v}$ is the velocity vector, k is the fluid thermal conductivity and $\dot{q}_V$ is the volumetric thermal energy generation.

The following assumptions were considered: 1) steady state, 2) negligible heat generation (viscous dissipation), 3) laminar, incompressible and fully developed flow, 4)

velocity only in the axial direction (v_z), 5) negligible axial diffusion of heat and mass, 6) homogeneous local convective heat transfer coefficient along the tube circumference, 7) 2D axisymmetric problem around the z axis with $T = T(z,r)$ and $v = v(r)$ and 8) constant thermophysical properties evaluated at an average temperature. Consequently, Eq. (7) showed to be analogous to the Graetz problem for heat transfer in tubular laminar flow:

$$v_z \frac{\partial T}{\partial z} = \alpha \frac{1}{r} \frac{\partial}{\partial r}\left(r \frac{\partial T}{\partial r}\right) \tag{7}$$

where $\alpha = k/(\rho\, C_p)$ is the thermal diffusivity and $v_z(r)$ is the axial velocity profile.

Three boundary conditions are required to solve Eq. (7): specification of the tube inlet temperature, symmetry condition at the center of the tube and homogeneous convective heat transfer on the surface of the tube; the latter being a modification of the Graetz problem that considers constant wall temperature. The boundary conditions are summarized in Eq. (8) as:

$$\begin{cases} \text{For } z = 0 \rightarrow T(z,r) = T_{in} \\ \text{For } r = r_i \rightarrow -kA_i \dfrac{\partial T}{\partial r} = h_e A_e [T(z,r) \pm T_e] \\ \text{For } r = 0 \rightarrow \dfrac{\partial T}{\partial r} = 0 \end{cases} \tag{8}$$

where r_i is internal radius of the tube, A_i is the internal surface area of the tube, A_e is the external surface area of the tube, h_e is the average convective heat transfer coefficient of the external fluid over the tube wall and T_e is the temperature of the external fluid, which was considered uniform. In Eq. (8), the radial temperature gradient in the tube wall was neglected because of the low thermal resistance of the metal; nevertheless, this condition can be modified with the use of an overall heat transfer coefficient that considers the thermal resistances of the wall and of the external fluid.

225 **2.1 Heat transfer enhancement**

226 In a coiled tube, secondary flow due to the curves increases heat transfer within
227 the fluid. In order to increase the heat transfer rate in the 2D straight tube model, an
228 effective thermal diffusivity (α_{eff}) in the radial direction was used in Eq. (7), which is
229 based on an effective thermal conductivity (k_{eff}), since $\alpha_{eff} = k_{eff}/(\rho\, C_p)$. This
230 empirical parameter can be determined by heat transfer experiments, which are discussed
231 in section 3 using the approach from Morais and Gut [36].

232 A heat transfer enhancement factor (F) was defined as in Eq. (9) in terms of the
233 ratio of thermal diffusivities or thermal conductivities, comparing the fluid property (α or
234 k) with the effective values (α_{eff} or k_{eff}).

$$F = \frac{\alpha_{eff}}{\alpha} = \frac{k_{eff}}{k} \tag{9}$$

235 For high coil pitches or high coil diameters, the F value is expected to tend to
236 unity, since the geometry approximates a straight tube and the effect of secondary flow
237 (Dean vortices) is reduced.

238 The enhancement in heat transfer from the Dean vortices comes with a pressure
239 drop penalty. For pressure drop evaluation using the 2D model, it could be calculated for
240 laminar flow in a straight tube using Hagen-Poiseuille's equation (taking into account any
241 height difference between tube inlet and outlet), but using an enhancement factor ε to
242 increase the straight friction factor:

$$\varepsilon = \frac{f_{eff}}{f} \tag{10}$$

243 where f_{eff} is the effective friction factor obtained from experiments with the coiled tube,
244 f is the theoretical flow friction for laminar in straight tube with smooth walls. This
245 approach was successfully used by Rainieri et al. [40] to evaluate friction factor increase
246 in coiled tubes with and without wall corrugation.

2.2 Modified velocity profiles for laminar flow

The laminar velocity profile in a straight tube is not adequate to represent the flow in a coiled tube, since the secondary flow modifies the RTD by narrowing the dispersion in the E-curve [11]. In order for the 2D straight tube model to have the same RTD of the coiled tube it represents, modified laminar velocity profiles are proposed herein. They consist of modifications on the shape of the parabolic Newtonian velocity profile $v^* = 1 - r^{*2}$, which comes from the application of continuity and motion equations to describe steady-state fully developed isothermal laminar flow of a Newtonian fluid in a straight tube [41], where $r^* = r/r_i$ is the dimensionless radius and $v^* = v_z/v_{max}$ is the dimensionless velocity.

Four alternative velocity profiles and their corresponding RTD models were selected based on the work from Pegoraro et al. [41]. Fig. 2 presents the shape of the velocity profiles, as affected by the model parameters. Since flow is unidimensional and incompressible, these profiles satisfy the continuity equation for mass conservation. The laminar velocity profile of the straight tube was modified so that its theoretical RTD matches the RTD obtained from experiments with the coiled tube. The proposed velocity profiles and their corresponding RTD models are summarized in Table 1, where $\theta_0 = v_b/v_{max}$ is the dimensionless breakthrough time or first appearance time, $\theta = t/t_m$ is the dimensionless time, t_m is the mean residence time and $E_\theta(\theta)$ is the dimensionless exit age distribution function. The RTD function were derived directly from the velocity profiles without considering radial or axial diffusivity. In coiled tubes, the breakthrough time has shown to be higher than in straight tubes, e.g., the first appearance of the tracer is delayed due to the presence of secondary flow [42].

The y-laminar RTD model is based on the time-smoothed velocity profile characteristic of turbulent flow in tubes, which can be obtained with $y = 1/7$. Parameter

y varies between 0 and 1, and the piston flow condition is obtained when it approaches 0 [41]. The m-laminar RTD model is based on the laminar flow of a power-law fluid in a tube. The power-law velocity profile equation was generalized by introducing the parameter $m > 1$ as the exponent of r^*. As the value of m increases, the velocity profile gets flatter (piston flow), while the classic Newtonian profile is obtained with $m = 2$ [41].

A sinusoidal velocity profile was also suggested to represent non-ideal laminar flow in tubes. A cosine function was scaled to fit the (0,0)–(1,1) square of the $v^* \times r^*$ plot and the exponent α was introduced as a parameter. As the value of α decreases, the velocity profile gets flatter (piston flow) and a very close match of classic Newtonian profile is obtained with $\alpha = 0.430$. An exponential velocity profile was additionally proposed to represent non-ideal laminar flow in tubes. The exponential function was scaled to fit the (0,0)-(1,1) square of the $v^* \times r^*$ plot and the exponent β was introduced as a parameter. As the value of β decreases, the velocity profile gets flatter (piston flow).

RTD experiments with the coiled tube provide the E-curve, as further described in Section 3.1. The RTD models in Table 1 will then be adjusted in order to match this experimental E-curve. The velocity profile $v(r)$ corresponding the best match is going to be substituted in eq. (6) as v_z, thus changing the RTD of the 2D straight tube to mimic the RTD from the coiled tube. The experimental RTD is generally obtained under isothermal conditions at room temperature. In the proposed 2D straight tube model, it was assumed that the velocity profiles adjusted from the experimental RTD data are not significantly affected by temperature changes (effect of temperature on viscosity and density were not considered).

3. MATERIAL AND METHODS

In order to test and to validate the proposed model, the stainless-steel helically coiled tube shown in Fig. 3 (Armfield, Hampshire, UK) was used in experiments. The

297 tube has the following dimensions: internal diameter $d_i = 9.3$ mm, external diameter
298 $d_e = 12.7$ mm, diameter of the coil $d_c = 107$ mm, pitch $p = 12.7$ mm and nine turns ($n =$
299 9).

300 The calculated linear length of the helically coiled tube included the helix length
301 calculated with Eq. (4), the length of the straight tube section at the inlet (measured with
302 a tape measure) and the length of the curved tube at the outlet calculated with Eq. (4),
303 assuming $n = 1/4$. Thus, the total linear length was $L = 2.85$ m and the calculated
304 internal volume was $V = 194$ mL.

305 Two model fluids with different rheological behaviors were chosen: 1) a
306 glycerin/water mixture with a glycerin mass fraction of 80 %, which is a Newtonian fluid,
307 and 2) a carboxymethylcellulose (CMC) aqueous solution with mass fraction 1 %, which
308 is a non-Newtonian pseudoplastic fluid (power law).

309 The thermophysical properties of pure water and pure glycerin were obtained from
310 Yaws [43] and the properties for the glycerin/water mixture were weighted based on the
311 volume fraction for k and ρ or on the mass fraction for C_p. The viscosity (μ) of the mixture
312 was obtained from Cheng [44].

313 Properties of CMC solution were obtained from Carezzato et al. [45]. The concept
314 of generalized viscosity (μ_g) was used for calculating the generalized Reynolds number
315 (Re_g) and the generalized Prandtl numbers (Pr_g). The generalized viscosity for power-
316 law flow in a duct is defined in Eq. (11) as:

$$\mu_g = K \cdot \xi^{n-1} \cdot \left(\frac{v_m}{d_{eq}}\right)^{n-1} \left(\frac{\varphi \cdot n + 1}{(\varphi + 1) \cdot n}\right)^{n} \tag{11}$$

317 where K is the consistency coefficient, n is the flow behavior index d_{eq} is the equivalent
318 diameter of the duct and ξ and φ are the geometrical parameters of the duct. For a circular

tube, $d_{eq} = 2r_i$, $\xi = 8$ and $\varphi = 3$ [46]. All thermophysical properties were calculated at the average temperature between measurements at the inlet and outlet of the tube.

Critical Reynolds number was evaluated for all the experiments to determine the flow regime. The transition from laminar flow to turbulent flow is delayed in coiled tubes because the Dean vortices reduces the axial dispersion and stabilizes the flow suppressing turbulent fluctuations [40]. The correlation used was proposed by El-Genk and Schriener [47] for coiled tube (Eq. 12), which is a function of the curvature ratio $\delta = d_i/d_c$ and valid for $0.001 < \delta < 0.124$. Values under the Re_{crit} indicate laminar flow.

$$Re_{crit} = 2300\ (1 + 51640\ \delta^{1.575})^{0.2} \quad (12)$$

First, RTD experiments at room temperature were necessary to adjust the velocity profile from RTD models. Next, heat exchange experiments were performed to obtain the outlet temperatures for different conditions. The product pump and the heat exchangers of the pasteurization unit Microwave Lab25-UHT/HTST EHVH (MicroThermics, Raleigh, USA) were used to provide the feed for the coiled tube at the desired flow rate and temperature.

3.1 Residence time distribution experiments

The RTD experiments were carried out by colorimetric method using methylene blue as tracer. The glycerin/water mixture and the CMC solution were pumped at room temperature (between 20 and 25 °C) and at four flow rates (0.5, 1.0, 1.5 and 2.0 L/min). Three repetitions were made for each flow rate.

The tracer used in the experiments was methylene blue dissolved in the carrier fluid (glycerin/water mixture or CMC solution) at the concentration of 160 mg/L, which was introduced in the system by the pulse technique. A syringe with 1 mL capacity was used to perforate a silicone tube connected at the inlet of the coiled tube of Fig. 3 and 0.3 mL of tracer was quickly injected. Samples were collected at the outlet of the tube every

second and each sample was homogenized before spectrophotometric reading to measure the absorbance of the fluid (A). A spectrophotometer (model 700 Plus, FEMTO, São Paulo, Brazil) was used setting the wavelength to 665 nm with a quartz cuvette of 10-mm optical length.

The concentration of the tracer dissolved in the carrier fluid was tested to verify the validity of the Beer-Lambert law. Tests with both fluids showed that absorbance values were smaller than one ($A < 1$), thus, the Beer-Lambert law was valid in the RTD experiments (concentration of the tracer is proportional to the absorbance) [48]. Hence, the concentrations in the computation of $E(t)$ were replaced by the absorbances according to Eq. (13), where A_0 is the background absorbance and $A(t)$ is the absorbance of the sample. The integrals were numerically evaluated with the trapezoidal method.

$$E(t) = \frac{C(t) - C_0}{\int_0^\infty (C(t) - C_0)\, dt} = \frac{A(t) - A_0}{\int_0^\infty (A(t) - A_0)\, dt} \tag{13}$$

The four RTD models presented in section 2.2 (y-laminar, m-laminar, exponential and sinusoidal) were adjusted to the $E(t)$ values calculated from the experimental data. The parameter of each model and the corresponding mean residence time were iteratively adjusted by non-linear regression on $E(t)$, in terms of the minimization of the sum of squared errors ($MSSE$) between the experimental values ($E_{exp}(t)$) and the adjusted model ($E_{model}(t)$), as in Eq. (14).

$$MSSE = \min\left[\sum_{i=1}^{n} \left(E_{exp,i}(t) - E_{model,i}(t)\right)^2\right] \tag{14}$$

Starting with an initial guess for the model parameter (θ_0, y, m, α or β) and t_m, the SSE was minimized using the generalized reduced gradient method (GRG) in the Solver tool of Excel 2016 (Microsoft, Redmond, USA). The obtained RTD parameter was correlated with the volumetric flow rate and the correlation was later used for model simulation (Section 3.4).

365 **3.2 Cooling and heating experiments**

366 Cooling and heating experiments were conducted using an ultrathermostatic bath
367 with agitation (model MA184/30/-15A150 - Marconi, São Paulo, Brazil). The coiled tube
368 was immerged in hot or cold water, whilst the glycerin/water mixture or CMC solution
369 flowed inside the tube at flow rates of 0.5, 1.0, 1.5 and 2.0 L/min. An additional
370 mechanical agitator (model 715 - Fisatom, Brazil) was used to intensify mixing in the
371 bath.

372 Thermocouples with exposed junctions (IOPE, Brazil) were placed at the inlet
373 (T_{in}) and outlet (T_{out}) of the tube using union tees (John Guest, UK), and two other
374 thermocouples of the same type were placed in different regions of the water bath to
375 measure the external temperature (T_e). The experimental setup is shown in Fig. 4.

376 The thermocouples were connected to a cDAQ-9172 data acquisition system and
377 a computer running LabView data-logger code (National Instruments, Texas, EUA).
378 Once steady-state operation was verified, the temperatures were recorded every 1 s for 1
379 min. The experimental conditions are detailed in Table 2.

380 **3.3 Lumped capacitance experiments**

381 The coiled tube in the water bath was treated as a heat exchanger with convection
382 on the external surface, which means that the temperature on the surface of the tube was
383 not equal to the bulk temperature of the water bath ($T_w \neq T_e$). The wall boundary
384 condition for heat transfer on the wall (Eq. 8) requires the convective heat transfer
385 coefficient of the surrounding fluid over the external tube wall (h_e). The lumped
386 capacitance method was used to determine h_e experimentally, as an average value for the
387 whole surface of the coil.

388 This method consists of a transient heat transfer problem, in which a solid
389 experience a sudden change in its thermal environment and the change in the temperature

of the solid is registered in function of time. The main assumptions of the lumped capacitance method were: 1) uniform external temperature (T_e); 2) uniform convective heat transfer coefficient over the solid (h_e) and 3) the temperature of the solid was spatially uniform at any instant in time during the experiment, i.e., the temperature gradients within the solid were negligible [39].

The validity of the latter assumption can be verified by the Biot number (Bi), a dimensionless group defined in Eq. (15) as the ratio between the thermal resistances inside the solid (conduction) and at the interface with the fluid (convection):

$$Bi = \frac{h\ l}{k_s} \tag{15}$$

where k_s is the thermal conductivity of the solid, l is its characteristic length, calculated as the ratio between the solid volume ($V_s = \pi({r_e}^2 - {r_i}^2)L$) and its external superficial area ($A_e = 2\pi r_e L$). The assumption of uniform temperature in the solid is reasonable for small Biot numbers ($Bi < 0.1$) [39].

Considering a solid losing heat by convection to a fluid media in a situation of small Biot number, the overall energy balance on the solid yields Eq. (16).

$$\rho\ V\ C_p \frac{dT}{dt} = -h_e\ A_e\ (T - T_e) \tag{16}$$

Separating variables and integrating for an initial state t = 0 with the solid at the initial temperature T_i to an instant t with temperature $T(t)$, Eq. (17) is obtained. With experimental data of temperature as a function of time, the heat transfer coefficient of the surrounding fluid can be obtained by curve fitting.

$$\frac{T(t) - T_e}{T_i - T_e} = \exp\left(-\frac{h_e\ A_e}{\rho\ V\ C_p} t\right) \tag{17}$$

The empty coiled tube in Fig. 3, at a given initial temperature, was submerged in the ultrathermostatic water bath used in heating and cooling experiments, with the same

agitation conditions. For the heating experiment, the settings were T_i = 10 °C and T_e = 80 °C; while for the cooling experiment: T_i = 80 °C and T_e = 10 °C.

A thermocouple with exposed junction (IOPE, Brazil) was fixed in the middle part of the coil with thermal paste for better contact (k = 11 W.m^{-1}.K^{-1}). Temperature was recorded every second until the temperature of the tube reached the value of the external temperature (T_e). Next, parameter h_e in Eq. (17) was iteratively adjusted by non-linear regression, using the minimization of the sum of squared errors ($MSSE$) between $T(t)_{calc}$ and $T(t)_{exp}$. The value of T_i was as well adjusted (pseudo initial temperature) for a better curve fitting.

3.4 Model simulation

The 2D model proposed in Section 2, including the velocity profile adjusted from the RTD experiments (Table 1, Section 3.1), was solved by the finite difference method with the differential-algebraic solver DASOLV built in software gPROMS 6.0.2 (Process Systems Enterprise, UK). The differential and algebraic equations for the model were inputted using the Model Builder interface. For domain discretization, the geometry domain was divided into rectangular elements to compose the mesh. An aspect ratio of 5.0 was considered for each element, i.e., the length of each rectangle was five times its height, because of the large length of the tube.

A mesh independency study was conducted to obtain a mesh independent solution, which is a way to reduce discretization errors [49]. The mixing cup temperature or bulk temperature (T_b) at the tube outlet was the variable selected for this study. The bulk temperature can be calculated in function of the axial position according to Eq. (18) [5].

$$T_b(z) = \frac{2}{v_b {r_i}^2} \int_0^{r_i} T(z,r) v_z(r)\, r\, dr \tag{18}$$

The details of the meshes tested are shown in Table 3. The mesh independency study was realized for both fluids (glycerin/water mixture or CMC solution), at flow rate

434 0.5 L/min and F = 1. The temperatures were based on the heating condition H1 and
435 cooling condition C4 because of the larger temperature differences. The best mesh was
436 obtained when the absolute error of temperature between simulations was lower than 0.1
437 °C.

438 After establishing the mesh, the simulations of the heating and cooling
439 experiments were performed. Equations (7) and (18) were discretized using the first order
440 backward finite difference for the axial components and with the second order centered
441 finite difference for the radial components.

442 Since the outlet bulk temperature is unknown before simulation, an initial guess
443 was needed for calculating the average thermo-physical properties (ρ, C_p and k). The
444 initial guess used for the outlet temperature was the experimental measurement. An
445 iterative procedure was used to converge the fluid outlet bulk temperature: 1) the 2D
446 model was solved for $T(z,r)$, 2) the outlet value of T_b was used to calculate the new
447 average temperature, and 3) the values of the thermophysical properties were updated.
448 Steps 1 to 3 were repeated until convergence for a precision of 0.1 °C on the outlet bulk
449 temperature.

450 To test the model, simulations were first carried out using given values of F to
451 determine the corresponding temperature profile $T(z,r)$ and the outlet bulk temperature
452 $T_b(z = L)$. Next, simulations were run specifying the experimental outlet temperatures
453 of the fluid obtained from the 32 experimental conditions in Table 2, while α_{eff} was set
454 as a free variable in the model. Then, the corresponding F value was calculated using Eq.
455 (9) and correlated with the Reynolds number. The diagram in Fig. 5 shows the
456 information flows between the experimental and simulation steps for adjusting the
457 parameters of the semi-empirical model and using the model to simulate heat and mass
458 transfer.

To verify results, the correlations for F were substituted in the 2D model and it was simulated to predict the outlet temperatures for the 32 heating and cooling experiments, which were compared with the measurements. Additionally, the Nusselt correlations from Janssen and Hoogendoorn [50] for laminar convective heat transfer in helical coiled tubes were used to predict the outlet temperatures for all heating and cooling experiments. Since different flow rates were considered, the range of Dean number vary between the upper and lower limits of Eqs. (19a) to (19c):

$$Nu = 1.7\,(De^2\,Pr)^{1/6} \qquad \text{for } De < 20 \tag{19a}$$

$$Nu = 0.9\,(Re^2\,Pr)^{1/6} \qquad \text{for } 20 < De < 1\times10^2 \tag{19b}$$

$$Nu = 0.7\,Re^{0.43}\,Pr^{1/6}\left(\frac{d_i}{d_c}\right)^{0.07} \qquad \text{for } 1\times10^2 < De < 8.3\times10^2 \tag{19c}$$

were $Nu = h\,d_i/k$ is the peripherally averaged asymptotic Nusselt number for the fully developed thermal region. The outlet temperature of the coiled tube then was calculated from:

$$\rho\,Q\,C_p\,|T_{out} - T_{in}| = U\,A_e\,\frac{(T_{out} - T_e) - (T_{in} - T_e)}{\ln\dfrac{(T_{out} - T_e)}{(T_{in} - T_e)}} \tag{20}$$

in which the left-side term is the heat transfer rate based on the temperature change of the stream and the right-side term is the heat load based on the log-mean temperature difference and on the overall heat transfer coefficient U [39]:

$$\frac{1}{U\,A_e} = \frac{1}{h\,A_i} + \frac{\ln\left({}^{d_e}/_{d_i}\right)}{2\pi\,L\,k_s} + \frac{1}{h_e\,A_e} \tag{21}$$

4. RESULTS AND DISCUSSION

The RTD experimental results are presented first, since the velocity profile in the model is defined according to the RTD model with the best fit, followed by the results

475 from the heating and cooling experiments and lumped capacitance experiments. Next, the
476 simulation results of the 2D model are presented and discussed.

477 **4.1 Results from the RTD experiments**

478 The average values of the sum of squared errors (SSE) of the RTD model
479 adjustment for the four flow rates (0.5, 1.0, 1.5 and 2.0 L/min) are shown in Table 4 for
480 the glycerin/water mixture and the CMC solution. The y-laminar model was considered
481 as the best fit because of the lowest value of SSE. An example of the y-laminar model
482 fitting to experimental RTD data is shown in Fig. 6A for the CMC solution and in Fig.
483 6B for the glycerin/water mixture, at the flow rate of 0.5 L/min. Consequently, the
484 velocity profile of the y-laminar model (Eq. 22) was included in the 2D model.

$$v_z(r) = v_{max}\left(1 - \frac{r}{r_i}\right)^y \tag{22}$$

485 A linear correlation was adjusted between the RTD parameter y and the flow rate,
486 as shown in Fig. 7A for the CMC solution, and in Fig. 7B for the glycerin/water mixture.
487 Values of y were smaller than one and linearly increased with the Reynolds number for
488 the Reynolds range herein. A similar behavior can be seen for the two fluids. The
489 correlations in Fig. 7 were used to obtain the values of y for Eq. (22), which varied from
490 0.12 to 0.31 for the CMC solution and from 0.11 to 0.39 for the glycerin/water mixture.

491 The critical Reynolds number for the laminar flow calculated with Eq. (12) was
492 9337. For all RTD experiments, the highest Reynolds number value was 112 for the
493 glycerin/water mixture and 61 for the CMC solution (generalized Reynolds number).
494 Since these values were below the critical Reynolds, the flow regime was assumed to be
495 laminar.

496 **4.2 Results from the cooling and heating experiments**

497 The results of the heating and cooling experiments are shown in Table 5 for the
498 CMC solution and in Table 6 for the glycerin/water mixture, in flow rates of 0.5, 1.0, 1.5

and 2.0 L/min. In total, 32 experiments without repetitions were carried out for each fluid, combining different conditions of flow rate, inlet temperature and external temperature (Table 2). Further in this work, the experimental outlet temperatures were specified as a boundary condition in the 2D model, setting α_{eff} as a free variable to be calculated in the simulations.

The Reynolds number for the experimental conditions was calculated using thermophysical properties calculated for the average temperature of the fluid $T_m = (T_{in} + T_{out})/2$. The range of Reynolds obtained for each experimental condition is shown in Table 7 for the glycerin/water mixture and in Table 8 for the CMC solution, along with the ranges of Dean number and viscosity (K and n for the CMC solution).

The highest Reynolds number was 892 for the glycerin/water mixture (Table 7) and 102 for the CMC solution (Table 8). The critical Reynolds number calculated by Eq. (12) was not exceeded ($Re_{crit} = 9337$); thus, the flow was assumed laminar in all experiments.

The Dean number varied from 20 to 263 for the glycerin/water mixture (Table 7) and from 3 to 30 for the CMC solution (Table 8). According to Dravid et al. [7], the secondary flow is significant for $De > 100$. This value was exceeded at the higher flow rates (1.5 L/min and 2.0 L/min) for the glycerin/water mixture; thus, the secondary flow effects may have been stronger in these cases.

4.3 Results from the lumped capacitance experiments

Results of the lumped capacitance method are shown in Fig. 8A for the heating experiment and in Fig. 8B for the cooling experiment, where $\theta = (T(t) - T_e)/(T_i - T_e)$ is the dimensionless temperature. A good fitting was obtained with a clear log-linear dependence between dimensionless temperature and time.

For the heating experiment, the adjusted value of the convective coefficient was h_e = 962 W·m^{-2}·K^{-1} with Bi = 0.11; for the cooling experiment, the adjusted value was h_e = 753 W·m^{-2}·K^{-1} with Bi = 0.08. The requirement of $Bi < 0.1$ of the lumped capacitance method was acceptable given the limiting value obtained. The values of h_e were used in the 2D model in the wall boundary condition of heat transfer.

4.4 Simulations and model validation

Results of the model mesh refinement study are shown in Table 9 for the CMC solution, Q = 0.5 L/min and F = 1. The absolute errors for outlet temperature were lower than 0.1 °C for meshes M9 and M10, which were considered acceptable for this study. Mesh M10 with 1000 axial points and 200 radial points was then selected to represent the computational domain because of the small relative error of temperature and the small computational time (ca. 1 min). Similar results were obtained with the glycerin/water mixture.

The 2D model was simulated for the 32 experimental conditions in Table 2, using the velocity profile of the y-laminar model and the correlations in Fig. 7 to calculate the value of y. First, different values of F (1.0 and 3.0) were tested to verify its influence on the bulk temperature along the tube length, as shown in Fig. 9A for heating condition H1 and in Fig. 9B for cooling condition C2. When $F = 1$, the effective thermal diffusivity is equal to the fluid property ($\alpha_{eff} = \alpha$); when setting $F = 3$, the heat transfer rate was increased up to 93 % for the glycerin/water mixture and up to 99% for the CMC solution in comparison to the base case.

Another analysis was conducted to verify the influence of the enhancement factor on the radial temperature profile at the tube outlet, for the experimental conditions H1 (Fig. 10A) and C2 (Fig. 10B). Flatter temperature profiles (small difference between

547 center and wall temperatures) can be observed as F increases, because of the higher heat
548 transfer rate.

549 Simulations of the 2D model with the specification of the experimental outlet
550 temperatures provided the values of α_{eff}. The corresponding F values were calculated
551 using Eq. (8), which varied from 0.84 to 2.62 for the CMC solution and from 1.25 to 3.18
552 for the glycerin/water mixture.

553 The F values were correlated with the Reynolds number in log scale, as shown in
554 Fig. 11. It was possible to group data from both fluids in a single plot; however, the
555 combination of heating and cooling experiments in Fig. 11C increased the scattering of
556 points and was not considered appropriate. The dispersion of points seen in Fig. 11 may
557 be related to the assumption that the velocity profile derived from the experimental RTD
558 was valid at all temperatures in the experiments, since viscosity has an important
559 temperature dependence and affects flow. Trends show that the value of F tends to unity
560 with decreasing Reynolds number, with a limiting Reynolds at $F = 1$. This was expected,
561 since the influence of secondary flow becomes negligible for decreasing Reynolds and
562 Dean numbers. The linear log-log correlation in Fig. 11A is valid for $Re \geq 6.8$ and the
563 correlation of Fig. 11B is valid for $Re \geq 16.1$ (F = 1 for lower values). As Dean numbers,
564 these thresholds are $De \geq 2.0$ (heating) and $De \geq 4.7$ (cooling), which are lower than the
565 limit of 20, under which the heat transfer enhancement is negligible according to Dravid
566 et al. [7].

567 The adjusted F correlations in Fig. 11A and 11B were substituted in the model,
568 and the experimental conditions were simulated to calculate the outlet bulk temperature
569 for all the heating and cooling experiments in Table 2 to evaluate the model prediction
570 error for outlet temperature. Additionally, the Janssen and Hoogendoorn [50] correlations
571 in Eqs. (19a) to (19c) were used to predict the outlet temperatures. The range of Dean

572 numbers presented in Tables 7 and 8 confirmed that Eqs. (19a) to (19c) were used for the
573 glycerin/water mixture, while for the CMC solution only Eqs. (19a) and (19b) were used.
574 The values obtained were compared with the measured outlet temperatures, as
575 shown in the parity charts in Fig. 12 for the CMC solution (Fig. 12A) and for the
576 glycerin/water mixture (Fig. 12B). A good agreement between experimental and
577 simulated values was obtained for the CMC solution with the $R^2 = 0.939$ and all
578 deviations under 5 °C. Predictions from the Nusselt correlations had $R^2 = 0.647$ with 11
579 conditions with deviations over 5 °C. For the glycerin/water mixture, the errors were
580 larger, yielding $R^2 = 0.791$, but with most of the deviations under 5 °C. Predictions from
581 Nusselt correlations were mostly over 5 °C, as can be seen in Fig. 12A.
582
583 **5. CONCLUSIONS**
584 The proposed 2D semi-empirical model allowed the determination of the velocity
585 and temperature fields inside the straight tube in a way that its RTD mimics the E-curve
586 of the coiled tube, and the predicted outlet temperature matches the experimental value
587 using a heat transfer enhancement factor. This model depends on inputting two
588 parameters: y and F, which were obtained from experiments using two model fluids with
589 different rheological behavior. Velocity profile parameter y was correlated with the flow
590 rate (Reynolds was not used since temperature effects were neglected for the RTD) and
591 provided a flatter profile in comparison with the theoretical laminar profile for a straight
592 tube. Heat transfer enhancement factor F linearly correlated with the Reynolds number
593 in a log-log plot, combining data from the two model fluids, but with a small difference
594 in trend between the heating and cooling experiments. These plots provided a threshold
595 value for negligible heat transfer enhancement in the coiled tube.

Simulation time for this 2D model was very small in comparison with the values expected for typical 3D CFD simulations, and it can provide a reliable outlet temperature for the coiled heat exchanger (Fig. 12). The advantage of this approach over using Nusselt correlations to predict the outlet temperature is that the 2D model provides velocity and temperature fields in the tube that can be used for the simulation of non-isothermal reactions. The downside of the model is the previous requirement of experiments to provide correlations for y and F. In the case of design changes, a new set of parameters will be necessary. Some ideas for further investigation of this 2D modeling approach would be: 1) this model could use virtual experiments from a rigorous 3D model in CFD to adjust not only the outlet temperature, but the bulk temperature distribution along the tube as well; 2) to study the dependence of RTD parameter y with temperature, thus correlating it with the Reynolds number; 3) to use this approach to model a corrugated coiled tube so y and F would take into account two passive heat transfer enhancement techniques; 4) to introduce the differential species mass balance equation in the model to evaluate a non-isothermal LFR in a coiled tube to predict not only temperature distribution, but reaction yield as well, as in the bacterial inactivation in thermal processing of liquid foods.

DECLARATION OF COMPETING INTEREST

The authors declare that they have no known competing financial interests or personal relationships that could have appeared to influence the work reported in this paper.

DATA AVAILABILITY

Data will be made available on request.

ACKNOWLEDGEMENTS

This research was supported by Fundação de Amparo à Pesquisa do Estado de São Paulo – FAPESP (grants 2006/01628-0, 2013/07914-8), Conselho Nacional de Desenvolvimento Científico e Tecnológico – CNPq (grants 140573/2019-4, 316388/2021-1) and Coordenação de Aperfeiçoamento de Pessoal de Nível Superior – CAPES (Finance Code 001).

ORCID

Nilo H. M. Fortes - https://orcid.org/0000-0003-1763-8329

Artemio Plana-Fattori - https://orcid.org/0000-0001-8326-7007

Jorge A. W. Gut - https://orcid.org/0000-0001-6447-8490

REFERENCES

[1] M. Mansour, Z. Liu, G. Janiga, K.D.P. Nigam, K. Sundmacher, D. Thévenin, K. Zähringer, Numerical study of liquid-liquid mixing in helical pipes, Chem. Eng. Sci. 172 (2017) 250–261. https://doi.org/10.1016/j.ces.2017.06.015

[2] P. Vocale, F. Bozzoli, S. Rainieri, G. Pagliarini, Influence of thermal boundary conditions on local convective heat transfer in coiled tubes, Int. J. Therm. Sci. 145 (2019) 106039. https://doi.org/10.1016/j.ijthermalsci.2019.106039

[3] W.R. Dean, LXXII. The stream-line motion of fluid in a curved pipe (Second paper), London, Edinburgh, Dublin Philos. Mag. J. Sci. 5 (1928) 673–695. https://doi.org/10.1080/14786440408564513

[4] A. Aldor, Y. Moguen, K. El Omari, C. Habchi, P. Cocquet, Y. L, Y. Le Guer, Heat transfer enhancement by chaotic advection in a novel sine-helical channel geometry, Int.

645 J. Heat Mass Transf. 193 (2022) 122870.
646 https://doi.org/10.1016/j.ijheatmasstransfer.2022.122870
647 [5] R.B. Bird, W.E. Stewart, E.N. Lightfoot, Transport phenomena, 2nd ed., John
648 Wiley & Sons Inc, New York, 2002.
649 [6] K. Sandeep, P. Coronel, Flow Dynamics and Heat Transfer in Helical Heat
650 Exchangers, in: Transp. Phenom. Food Process., CRC Press, Boca Raton, 2003: pp. 377–
651 397. https://doi.org/10.1201/9781420006261.ch25
652 [7] A.N. Dravid, K.A. Smith, E.W. Merrill, P.L.T. Brian, Effect of secondary fluid
653 motion on laminar flow heat transfer in helically coiled tubes, AIChE J. 17 (1971) 1114–
654 1122. https://doi.org/10.1002/aic.690170517
655 [8] H. Fellouah, C. Castelain, A. Ould El Moctar, H. Peerhossaini, A criterion for
656 detection of the onset of Dean instability in Newtonian fluids, European Journal of
657 Mechanics B/Fluids 25 (2006) 505–531.
658 https://doi.org/10.1016/j.euromechflu.2005.11.002
659 [9] O. Levenspiel, Chemical Reaction Engineering, 3rd ed., John Wiley & Sons Inc,
660 New York, 1999.
661 [10] H. Zhao, H.H. Bau, Effect of secondary flow on Taylor-Aris dispersion,
662 Analytical Chemistry 79 (2007) 7792–7798. https://doi.org/10.1021/ac701681b
663 [11] F. Florit, R. Rota, K.F. Jensen, Dispersion in coiled tubular reactors: A CFD and
664 experimental analysis on the effect of pitch, Chem. Eng. Sci. 233 (2021) 116393.
665 https://doi.org/10.1016/j.ces.2020.116393
666 [12] L. Sharma, K.D.P. Nigam, S. Roy, Single phase mixing in coiled tubes and coiled
667 flow inverters in different flow regimes, Chem. Eng. Sci. 160 (2017) 227–235.
668 https://doi.org/10.1016/j.ces.2016.11.034

669 [13] R.K. Shah, D.P. Sekulic, Fundamentals of Heat Exchanger Design, Wiley, 2012.
670 https://doi.org/10.1002/9781118403198.ch4
671 [14] J. Ahmed, M.S. Rahman, Handbook of Food Process Design, Wiley, 2012.
672 https://doi.org/10.1002/9781444398274
673 [15] D. Borse, J.V. Bute, A Review on Helical Coil Heat Exchanger, Int. J. Res. Appl.
674 Sci. Eng. Technol. 6 (2018) 492–497. https://doi.org/10.22214/ijraset.2018.2070
675 [16] N. Kushwaha, T.C. Kumawat, K.D.P. Nigam, V. Kumar, Heat Transfer and Fluid
676 Flow Characteristics for Newtonian and Non-Newtonian Fluids in a Tube-in-Tube
677 Helical Coil Heat Exchanger, Ind. Eng. Chem. Res. 59 (2020) 3972–3984.
678 https://doi.org/10.1021/acs.iecr.9b07044
679 [17] N.S. Reddy, S.G. Subramanya, K.C. Vishwanath, S. Kanchiraya, V. Satheesha,
680 M. Karthikeyan, Analysis of tube-in-tube copper helical heat exchanger to improve heat
681 transfer, Mater. Today Proc. 39 (2020) 879–887.
682 https://doi.org/10.1016/j.matpr.2020.11.043
683 [18] F. Bozzoli, L. Cattani, S. Rainieri, F.S.V. Bazán, L.S. Borges, Estimation of the
684 local heat-transfer coefficient in the laminar flow regime in coiled tubes by the Tikhonov
685 regularisation method, Int. J. Heat Mass Transf. 72 (2014) 352-361.
686 http://dx.doi.org/10.1016/j.ijheatmasstransfer.2014.01.019
687 [19] W. Wang, Y. Zhang, K.S. Lee, B. Li, Optimal design of a double pipe heat
688 exchanger based on the outward helically corrugated tube, Int. J. Heat Mass Transf. 135
689 (2019) 706–716. https://doi.org/10.1016/j.ijheatmasstransfer.2019.01.115
690 [20] H.M. Maghrabie, M. Attalla, A.A.A. Mohsen, Performance of a shell and helically
691 coiled tube heat exchanger with variable inclination angle: Experimental study and
692 sensitivity analysis, Int. J. Therm. Sci. 164 (2021) 106869.
693 https://doi.org/10.1016/j.ijthermalsci.2021.106869

694 [21] D. Raut, S. Lanjewar, V.R. Kalamkar, Effect of geometrical and operational
695 parameters on paraffin's melting performance in helical coiled latent heat storage for solar
696 application: A numerical study, Int. J. Therm. Sci. 176 (2022) 107509.
697 https://doi.org/10.1016/j.ijthermalsci.2022.107509
698 [22] G. Wang, D. Wang, J. Deng, Y. Lyu, Y. Pei, S. Xiang, Experimental and
699 numerical study on the heat transfer and flow characteristics in shell side of helically
700 coiled tube heat exchanger based on multi-objective optimization, Int. J. Heat Mass
701 Transf. 137 (2019) 349–364. https://doi.org/10.1016/j.ijheatmasstransfer.2019.03.137
702 [23] Z. Lei, Z. Bao, Experimental investigation on laminar heat transfer performances
703 of RP-3 at supercritical pressure in the helical coiled tube, Int. J. Heat Mass Transf. (2021)
704 122326. https://doi.org/10.1016/j.ijheatmasstransfer.2021.122326
705 [24] B.R. Oliveira, B.C. Leal, L. Pereira Filho, R.F. de O. Borges, E. da C.H. Paraíso,
706 S. da C. Magalhães, J.M. Rocha, L.A. Calçada, C.M. Scheid, A model to calculate the
707 pressure loss of Newtonian and non-Newtonian fluids flow in coiled tubing operations, J.
708 Pet. Sci. Eng. 204 (2021). https://doi.org/10.1016/j.petrol.2021.108640
709 [25] Z. Xu, M. Liu, Y. Xiao, H. Gu, Development of a RELAP5 model for the thermo-
710 hydraulic characteristics simulation of the helically coiled tubes, Ann. Nucl. Energy. 153
711 (2021) 108032. https://doi.org/10.1016/j.anucene.2020.108032
712 [26] Y. Wang, J.L. Alvarado, W. Terrell, Thermal and flow characteristics of helical
713 coils with reversed loops, Int. J. Heat Mass Transf. 126 (2018) 670–680.
714 https://doi.org/10.1016/j.ijheatmasstransfer.2018.02.110
715 [27] M. Mansour, D. Thévenin, K. Zähringer, Numerical study of flow mixing and heat
716 transfer in helical pipes, coiled flow inverters and a novel coiled configuration, Chem.
717 Eng. Sci. 221 (2020) 115690. https://doi.org/10.1016/j.ces.2020.115690

718 [28] V.M. Hameed, F.J. Hamad, Implementation of novel triangular fins at a helical
719 coil heat exchanger, Chem. Eng. Process. - Process Intensif. 172 (2022) 108745.
720 https://doi.org/10.1016/j.cep.2021.108745
721 [29] L. Zheng, Y. Xie, D. Zhang, Numerical investigation on heat transfer and flow
722 characteristics in helically coiled mini-tubes equipped with dimples, Int. J. Heat Mass
723 Transf. 126 (2018) 544–570. https://doi.org/10.1016/j.ijheatmasstransfer.2018.05.111
724 [30] A.A.R. Darzi, M. Abuzadeh, M. Omidi, Numerical investigation on thermal
725 performance of coiled tube with helical corrugated wall, Int. J. Therm. Sci. 161 (2021)
726 106759. https://doi.org/10.1016/j.ijthermalsci.2020.106759
727 [31] J.C. Kurnia, B.A. Chaedir, A.P. Sasmito, Laminar convective heat transfer in
728 helical tube with twisted tape insert, Int. J. Heat Mass Transf. 150 (2020) 119309.
729 https://doi.org/10.1016/j.ijheatmasstransfer.2020.119309
730 [32] K.L. Liaw, J.C. Kurnia, A.P. Sasmito, Turbulent convective heat transfer in helical
731 tube with twisted tape insert, Int. J. Heat Mass Transf. 169 (2021) 120918.
732 https://doi.org/10.1016/j.ijheatmasstransfer.2021.120918
733 [33] M. Mansour, P. Khot, P. Kováts, D. Thévenin, K. Zähringer, G. Janiga, Impact of
734 computational domain discretization and gradient limiters on CFD results concerning
735 liquid mixing in a helical pipe, Chem. Eng. J. 383 (2020) 123121.
736 https://doi.org/10.1016/j.cej.2019.123121
737 [34] O.S. Galaktionov, P.D. Anderson, P.G.M. Kruijt, G.W.M. Peters, H.E.H. Meijer,
738 A mapping approach for three-dimensional distributive mixing analysis, Computer &
739 Fluids 30 (2001) 271–289. https://doi.org/10.1016/S0045-7930(00)00020-7
740 [35] O.S. Galaktionov, P.D. Anderson, G.W.M. Peters, H.E.H. Meijer, Mapping
741 approach for 3D laminar mixing simulations: application to industrial flows, Int. J. Num.
742 Methods in Fluids 40 (2002) 345–351. https://doi.org/10.1002/fld.290

743 [36] A.O. Morais, J.A.W. Gut, Determination of the effective radial thermal diffusivity
744 for evaluating enhanced heat transfer in tubes under non-Newtonian laminar flow,
745 Brazilian J. Chem. Eng. 32 (2015) 445–454. https://doi.org/10.1590/0104-
746 6632.20150322s00003318
747 [37] J.A.T.A. Dantas, J.A.W. Gut, Modeling sterilization value and nutrient
748 degradation in the thermal processing of liquid foods under diffusive laminar flow with
749 associations of tubular heat exchangers, J. Food Process Eng. 41 (2018) 1–13.
750 https://doi.org/10.1111/jfpe.12897
751 [38] E.W. Weisstein, “Helix.” From MathWorld--A Wolfram Web Resource., (2021).
752 https://mathworld.wolfram.com/Helix.html (accessed November 23, 2021).
753 [39] F.P. Incropera, D.P. Dewitt, T.L. Bergman, A.S. Lavine, Fundamentals of Heat
754 and Mass Transfer, 7th ed., John Wiley & Sons, Hoboken, New Jersey, 2011
755 [40] S. Rainieri, F. Bozzoli, L. Cattani, G. Pagliarini, Compound convective heat
756 transfer enhancement in helically coiled wall corrugated tubes, Int. J. Heat Mass Transf.
757 59 (2013) 353-362. https://doi.org/10.1016/j.ijheatmasstransfer.2012.12.037
758 [41] P.R. Pegoraro, M. Marangoni, J.A.W. Gut, Residence Time Distribution Models
759 Derived from Non-Ideal Laminar Velocity Profiles in Tubes, Chem. Eng. Technol. 35
760 (2012) 1593–1603. https://doi.org/10.1002/ceat.201200057
761 [42] A. Hopley, B.J. Doyle, D.M. Roberge, A. Macchi, Residence time distribution in
762 coil and plate micro-reactors, Chem. Eng. Sci. 207 (2019) 181–193.
763 https://doi.org/10.1016/j.ces.2019.06.016
764 [43] C.L. Yaws, Chemical Properties Handbook: Physical, Thermodynamic,
765 Environmental, Transport, Safety, and Health Related Properties for Organic and
766 Inorganic Chemicals, McGraw-Hill, New York, 1999.
767 http://www.knovel.com/knovel2/Toc.jsp?BookID=49

768 [44] N.S. Cheng, Formula for the viscosity of a glycerol-water mixture, Ind. Eng.
769 Chem. Res. 47 (2008) 3285–3288. https://doi.org/10.1021/ie071349z
770 [45] A. Carezzato, M.R. Alcantara, J. Telis-Romero, C.C. Tadini, J.A.W. Gut, Non-
771 Newtonian heat transfer on a plate heat exchanger with generalized configurations, Chem.
772 Eng. Technol. 30 (2007) 21–26. https://doi.org/10.1002/ceat.200600294
773 [46] F. Delplace, J.C. Leuliet, Generalized Reynolds number for the flow of power law
774 fluids in cylindrical ducts of arbitrary cross-section, Chem. Eng. J. Biochem. Eng. J. 56
775 (1995) 33–37. https://doi.org/10.1016/0923-0467(94)02849-6
776 [47] M.S. El-Genk, T.M. Schriener, A Review and Correlations for Convection Heat
777 Transfer and Pressure Losses in Toroidal and Helically Coiled Tubes, Heat Transf. Eng.
778 38 (2017) 447–474. https://doi.org/10.1080/01457632.2016.1194693
779 [48] A.I. Vogel, Quantitative chemical analysis, 5th ed., John Wiley & Sons Inc, New
780 Jersey, USA, 1989. https://doi.org/10.1085/jgp.25.4.523
781 [49] S. Mazumder, Numerical methods for partial differential equations: Finite
782 difference and finite volume methods, Academic Press, Oxford, 2016.
783 [50] L.A.M. Janssen, C.J. Hoogendoorn, Laminar convective heat transfer in helical
784 coiled tubes, Int. J. Heat Mass Transf. 21 (1978) 1197–1206.
785

FIGURE CAPTIONS

Figure 1 – Representation of the geometry in the 2D axisymmetric model

Figure 2 – Dimensionless velocity profiles derived from laminar tube flow in function of the model parameter

Figure 3 – Geometrical characteristics of the coiled tube used in the experiments

Figure 4 – Experimental setup of the cooling/heating experiments

Figure 5 –Experimental and simulation steps for adjusting the parameters of the semi-empirical model

Figure 6 – Fitting of the y-laminar model to the experimental RTD data for the CMC solution (A) and for the glycerin/water mixture (B) at the flow rate of 0.5 L/min

Figure 7 – Parameter y in function of the volumetric flow rate for the CMC solution (A) and for the glycerin/water mixture (B)

Figure 8 – Results of the lumped capacitance experiments for the heating (A) and cooling (B) conditions

Figure 9 – Simulation results of the bulk temperature (T_b) in function of the axial position (z) at the flow rate of 0.5 L/min for F = 1 and for F = 3 in the heating condition H1 (A) and in the cooling condition C2 (B). Non-dashed lines represent the CMC solution and dashed lines represent the glycerin/water mixture

Figure 10 – Simulation results of the temperature profile at the tube outlet ($T_{z=L}$) in function of the radial position (r) at the flow rate of 0.5 L/min for F = 1 and for F = 3 in the heating condition H1 (A) and in the cooling condition C2 (B). Non-dashed lines represent the CMC solution and dashed lines represent the glycerin/water mixture

Figure 11 – Logarithm of the heat transfer enhancement factor (F) in function of the logarithm of the Reynolds number for the heating experiments (A), cooling experiments (B) and assembled results (C). Triangles represent the CMC solution for heating (filled

811 triangles) and cooling cases (empty triangles), while circles represent the glycerin/water
812 mixture for the heating (filled circles) and cooling cases (empty circles).
813 **Figure 12** – Parity charts for predicting the outlet temperature of the CMC solution (A)
814 and the glycerin/water mixture (B) with the 2D model and using Nusselt correlations from
815 literature. Dashed lines indicate deviations of ±5 %.
816

817 **TABLE CAPTIONS**

818 **Table 1** – Details of the adjusted RTD models: velocity profiles, $E_\theta(\theta)$ functions,
819 parameters and breakthrough times. Adapted from [33]

820 **Table 2** – Conditions of the heating and cooling experiments for the glycerin/water
821 mixture and for the CMC solution: inlet temperatures, external temperatures and flow
822 rates

823 **Table 3** – Mesh independence study of the 2D axisymmetric model

824 **Table 4** – Sum of squared errors (SSE) between the adjusted RTD models and the
825 experimental data for the glycerin/water mixture and for the CMC solution

826 **Table 5** – Outlet temperatures obtained in the heating and cooling experiments for the
827 CMC solution

828 **Table 6** – Outlet temperatures obtained in the heating and cooling experiments for the
829 glycerin/water mixture

830 **Table 7** – Viscosity, Reynolds number and Dean number ranges of the heating and
831 cooling experiments with the glycerin/water mixture for the flow rates of 0,5 to 2,0 L/min

832 **Table 8** – Viscosity, Reynolds number and Dean number ranges of the heating and
833 cooling experiments with the CMC solution for the flow rates of 0,5 to 2,0 L/min

834 **Table 9** – Results of the mesh independence study for the CMC solution: outlet bulk
835 temperature, absolute errors of temperature and computational time

836

837 Figure 1

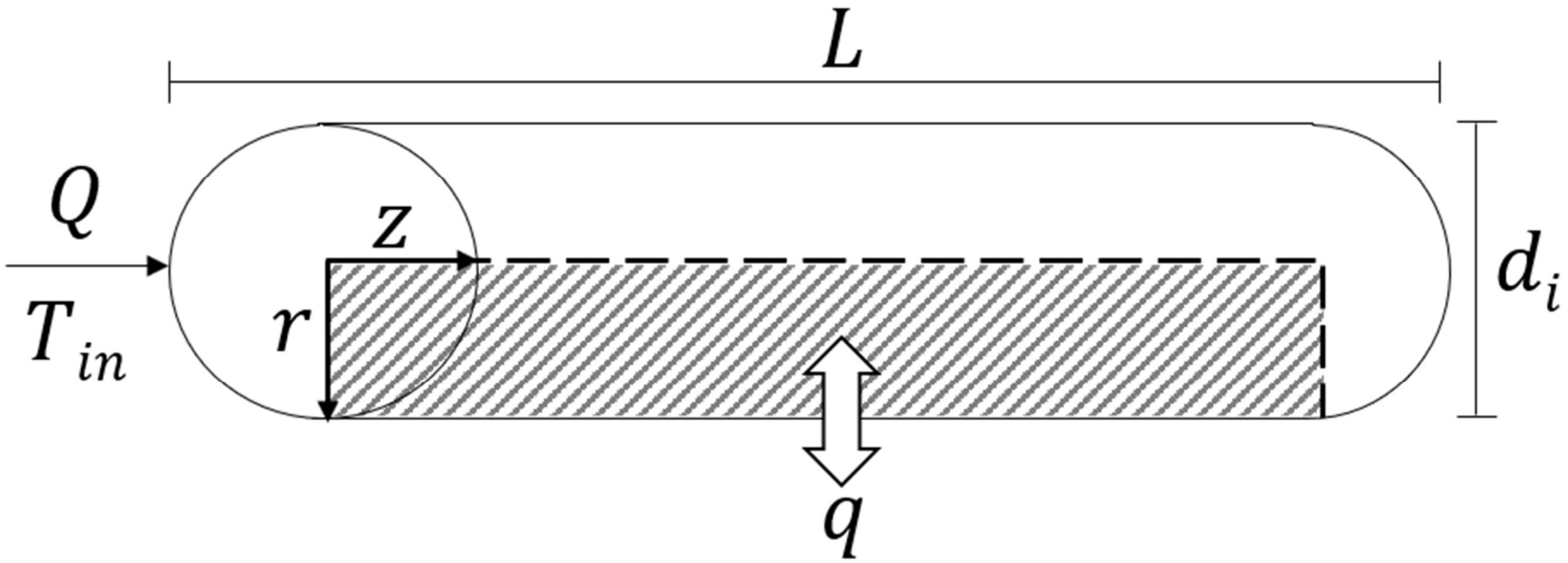

838

839 Figure 2

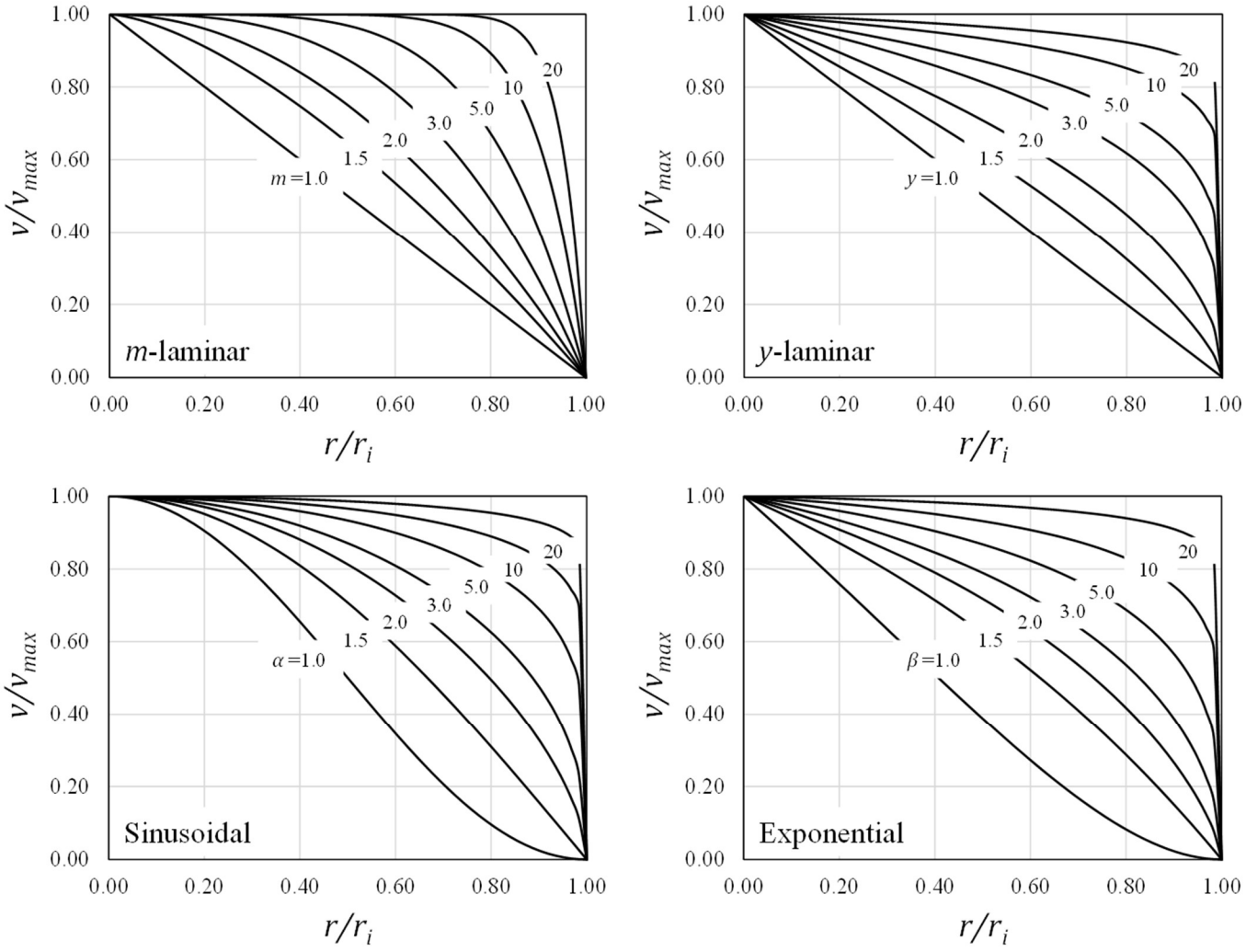

840

841 Figure 3

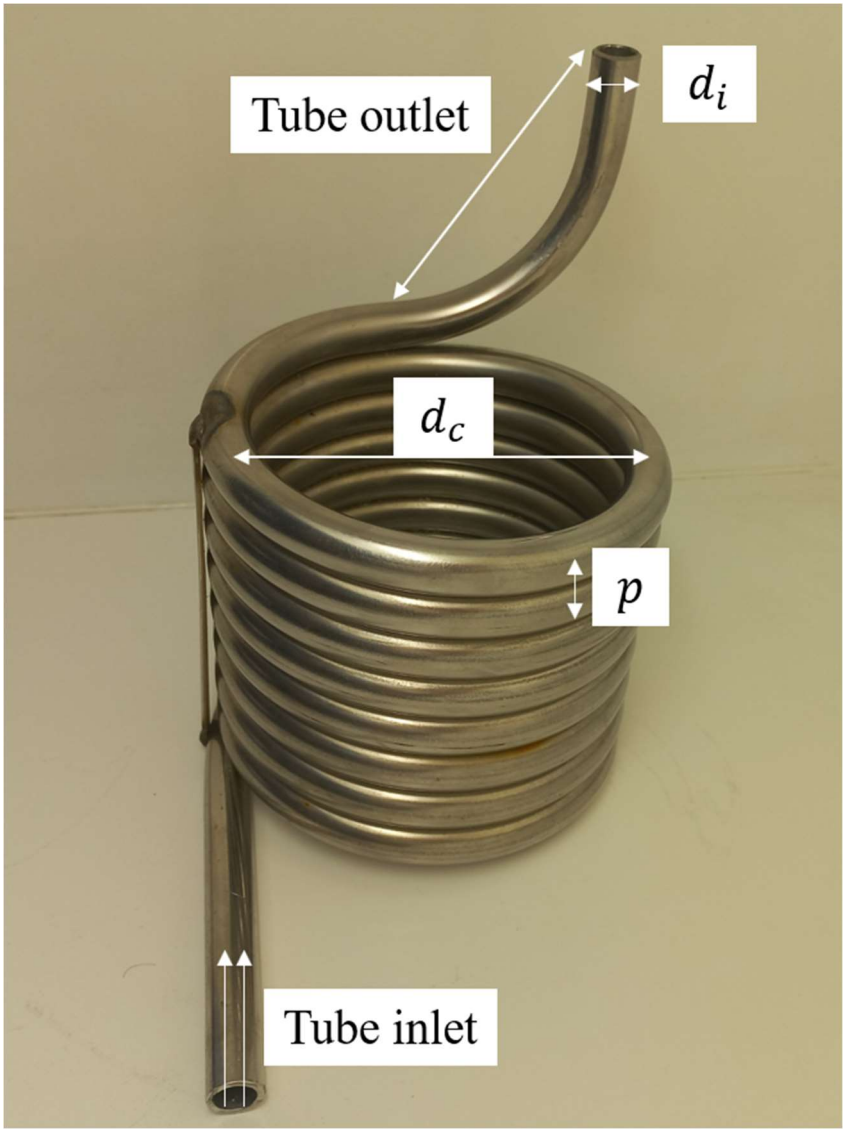

842

843 Figure 4

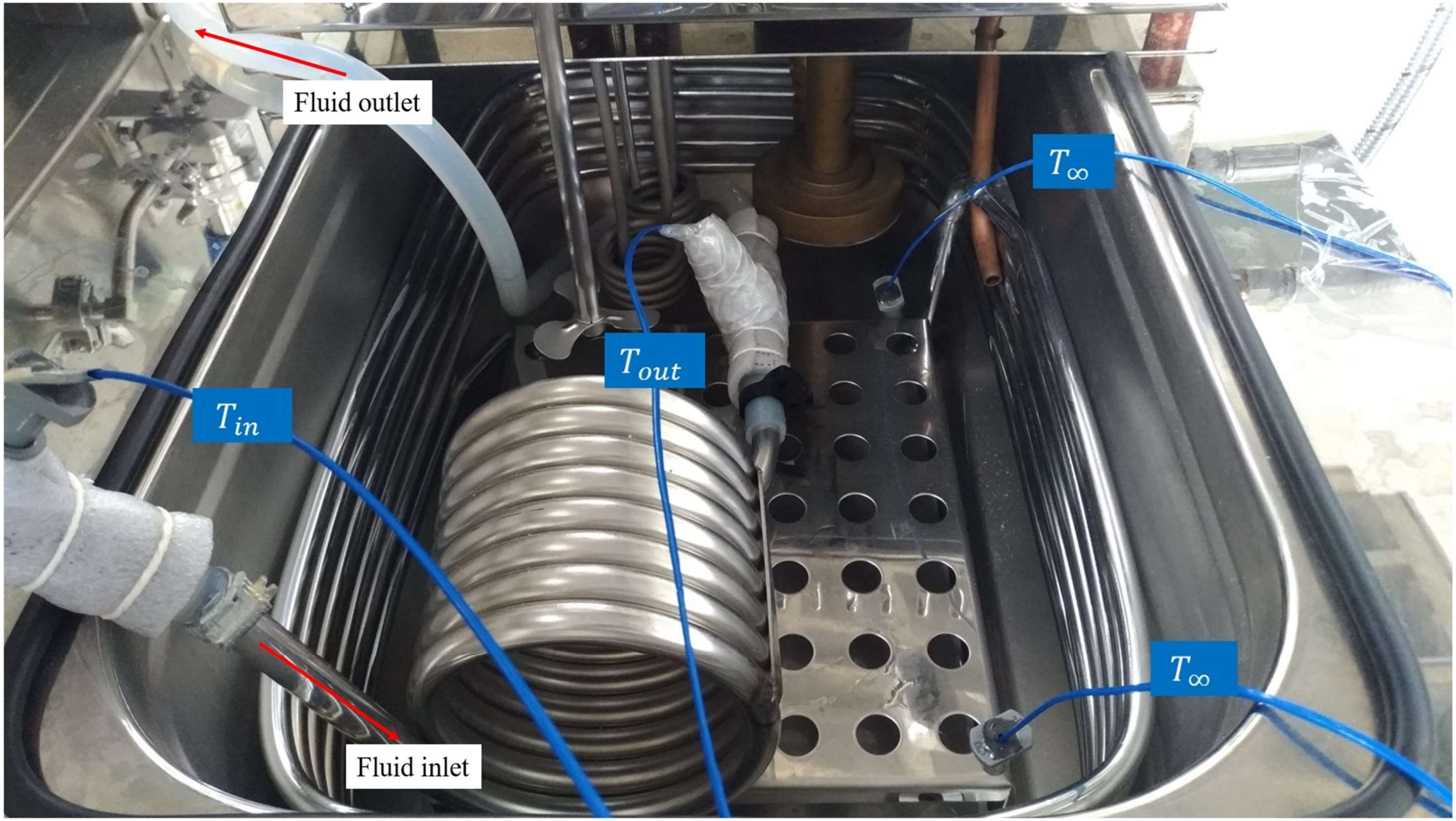

844

845 Figure 5

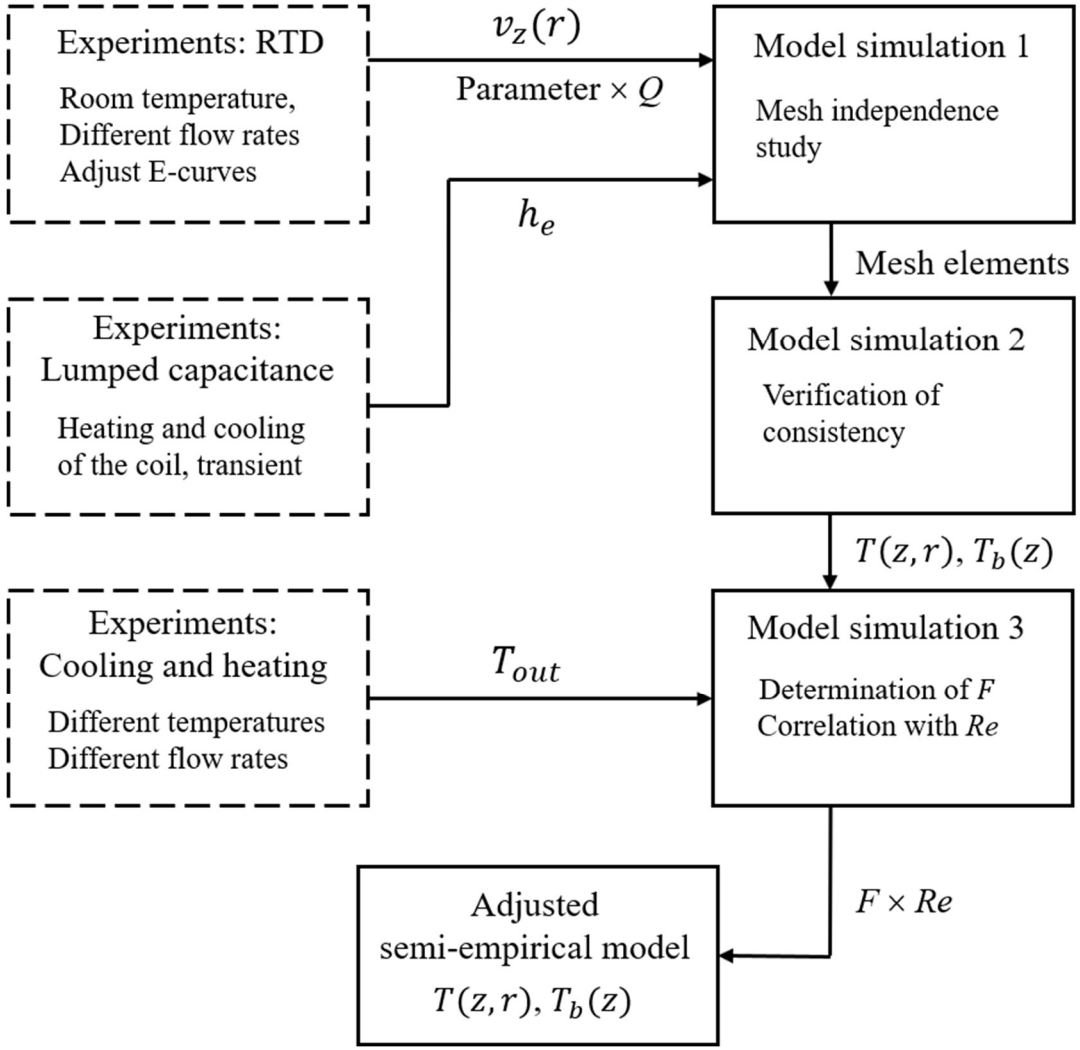

846

847 Figure 6

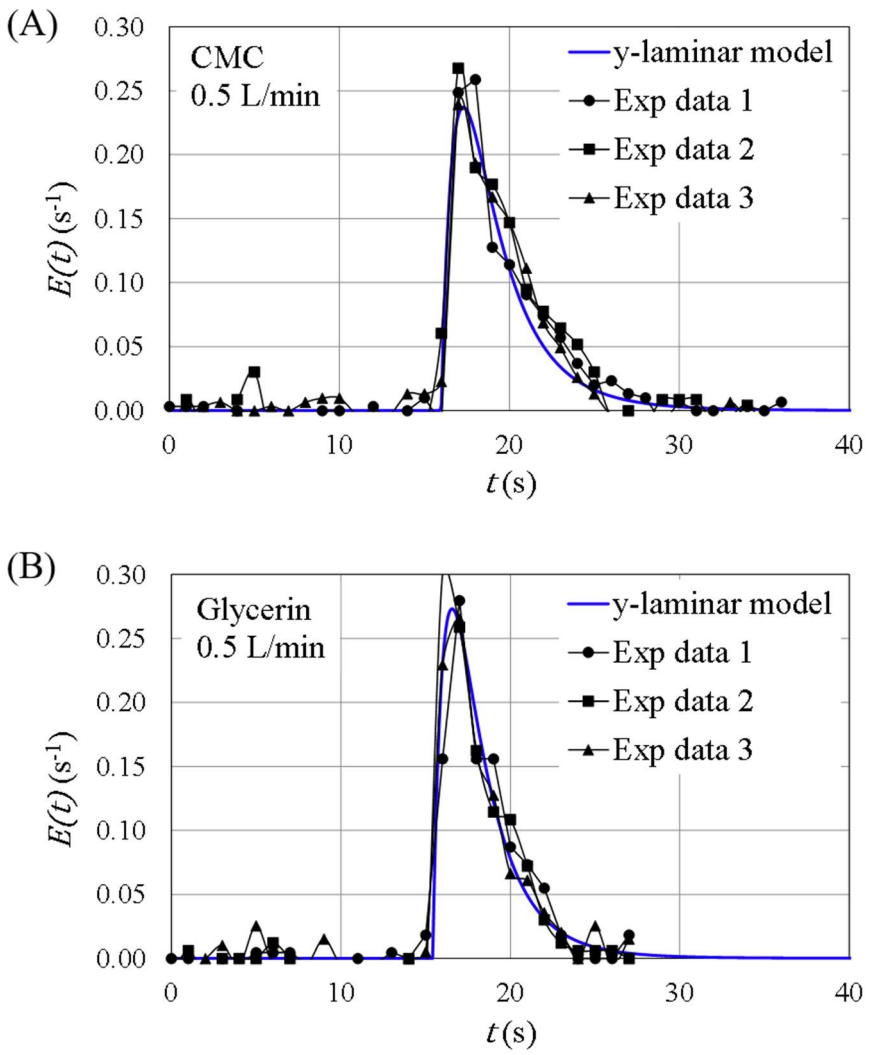

848

849

850 Figure 7

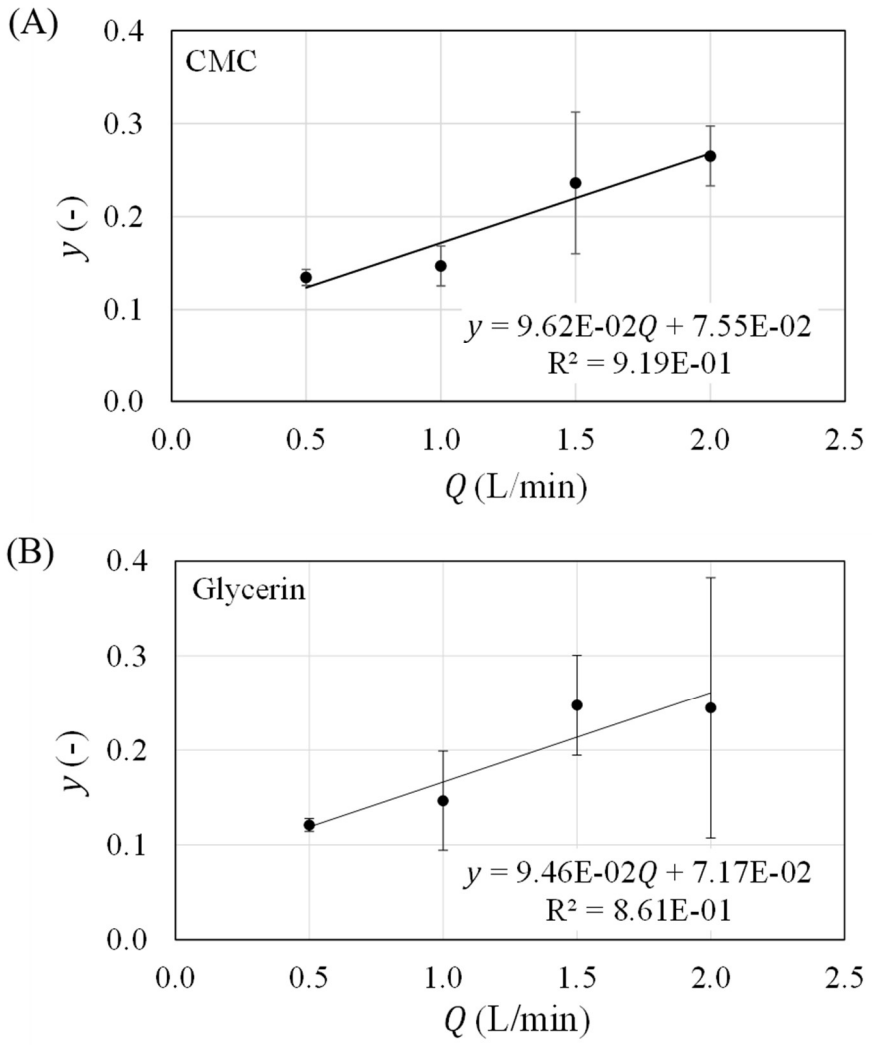

851

852 Figure 8

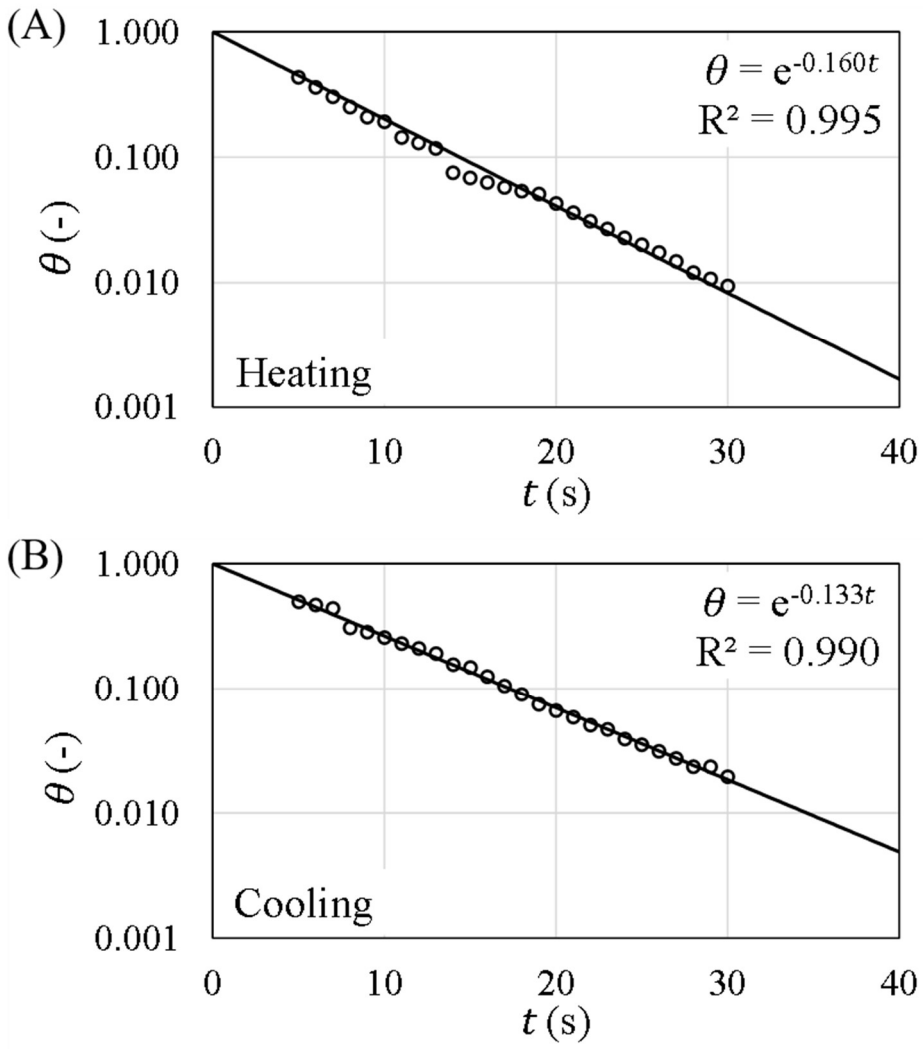

853

854 Figure 9

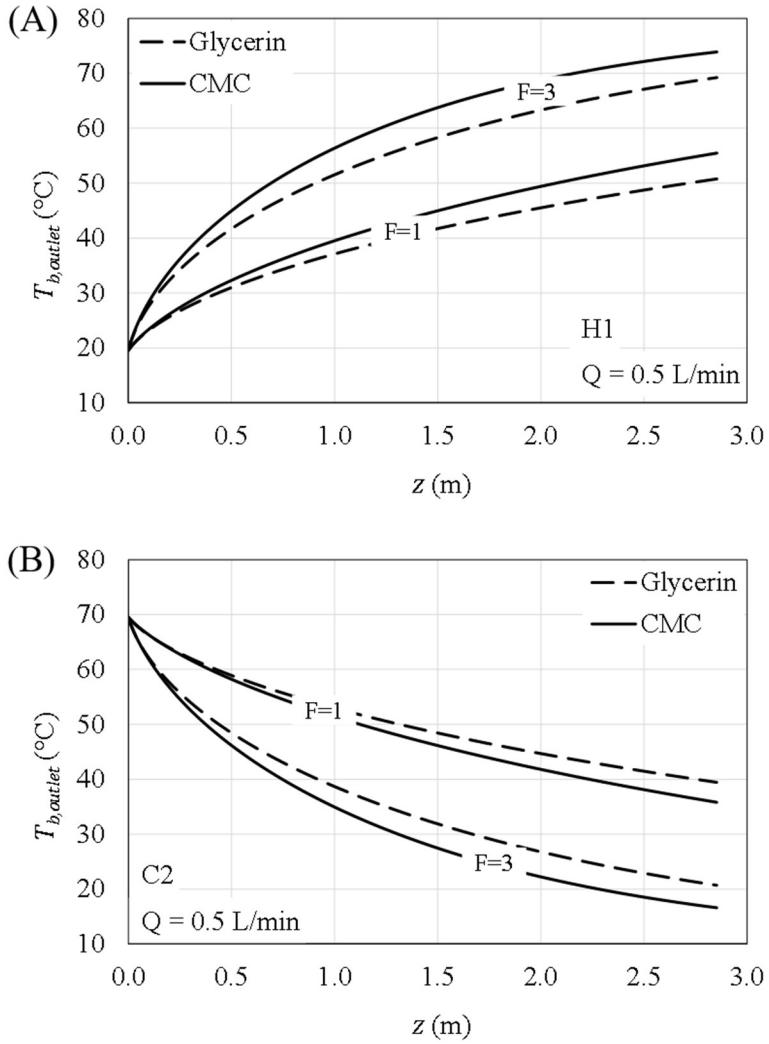

855

856 Figure 10

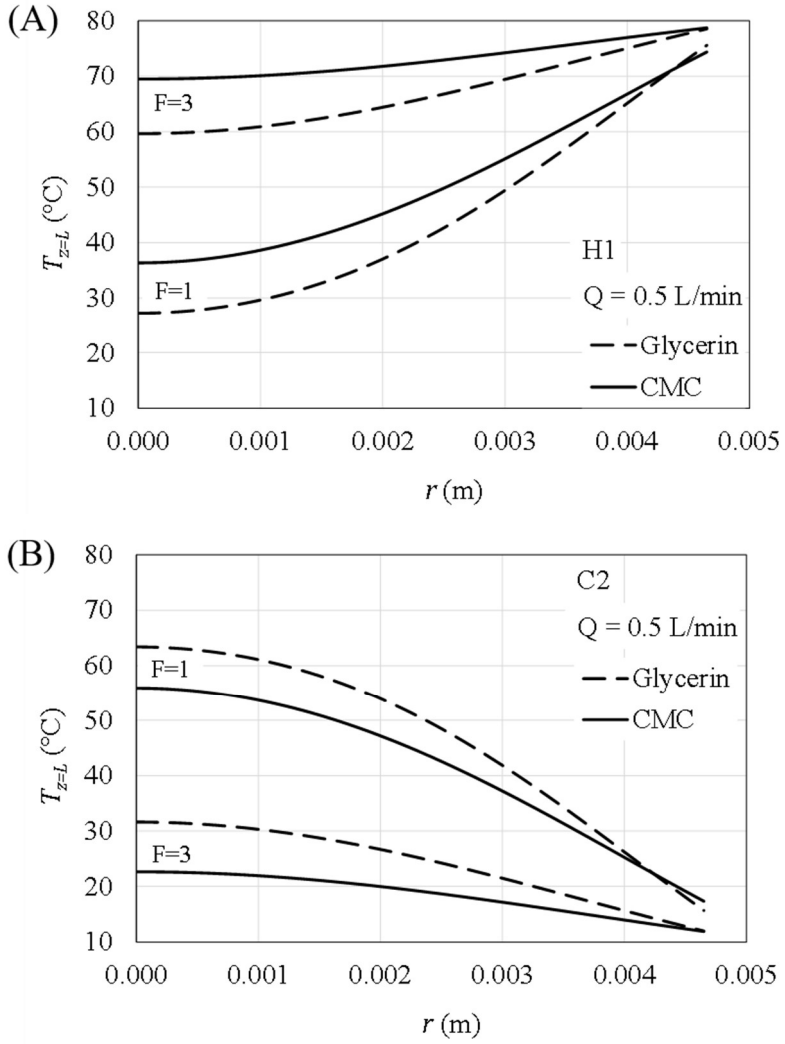

857

858

859 Figure 11

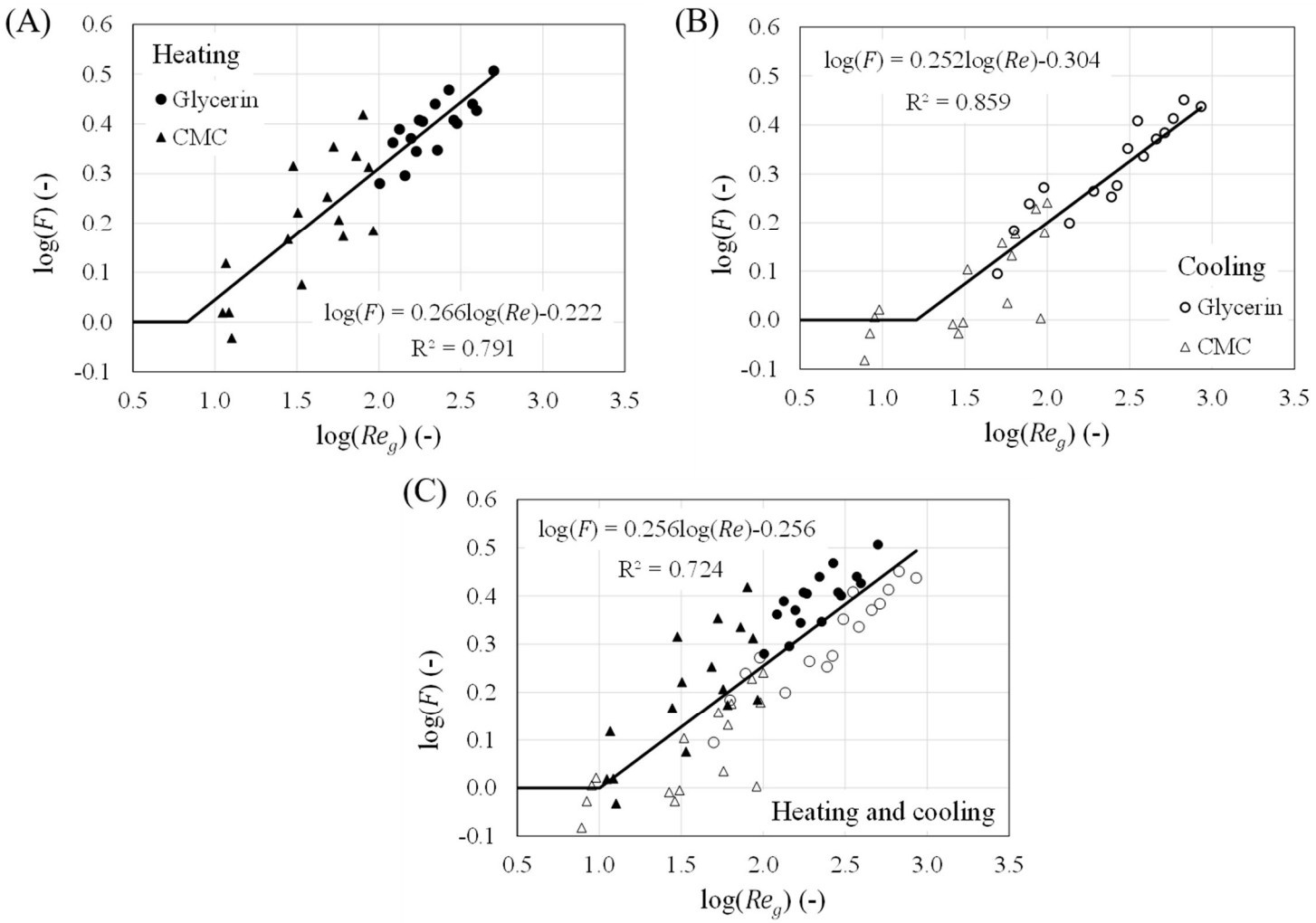

860

861 Figure 12

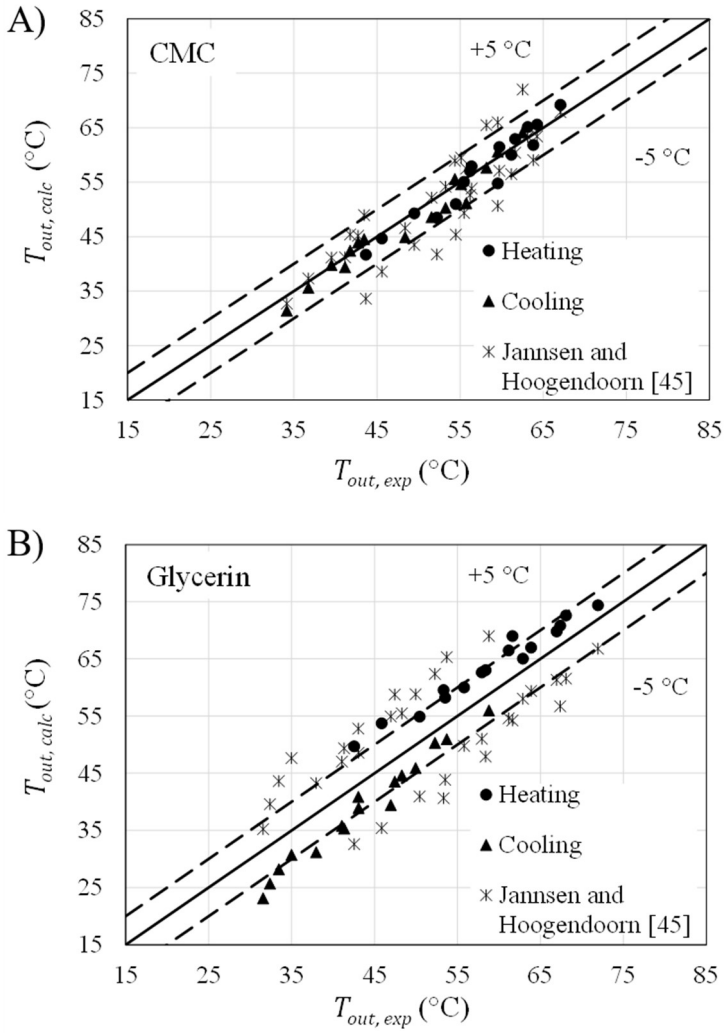

862

863 Table 1 – Details of the adjusted RTD models: velocity profiles, $E_\theta(\theta)$ functions, parameters and breakthrough times.

RTD Model	Velocity profile	RTD function	Parameter	Breakthrough time
m-laminar	$v^* = 1 - r^{*m}$	$E_\theta(\theta) = \frac{1}{\theta^3}\frac{2\theta_0}{m}\left(1 - \frac{\theta_0}{\theta}\right)^{\frac{2-m}{m}}$	m	$\theta_0 = \frac{m}{m+2}$
y-laminar	$v^* = (1 - r^*)^y$	$E_\theta(\theta) = \frac{1}{\theta^2}\frac{2}{y}\left(\frac{\theta_0}{\theta}\right)^{\frac{1}{y}}\left[1 - \left(\frac{\theta_0}{\theta}\right)^{\frac{1}{y}}\right]$	y	$\theta_0 = \frac{2}{y^2 + 3y + 2}$
Sinusoidal	$v^* = \left(\frac{1 + \cos(\pi r^*)}{2}\right)^\alpha$	$E_\theta(\theta) = \frac{1}{\theta^2}\frac{2}{\alpha\pi^2}\frac{\Phi}{\tan(\Phi/2)}$ with $\Phi = \operatorname{acos}\left[2\left(\frac{\theta_0}{\theta}\right)^{\frac{1}{\alpha}} - 1\right]$	α	$\theta_0 \approx \frac{{\alpha_0}^p}{\alpha^p + {\alpha_0}^p}$ $\alpha_0 = 0.43072$ $p = 1.0183$
Exponential	$v^* = \left(\frac{e - e^{r^*}}{e - 1}\right)^\beta$	$E_\theta(\theta) = \frac{1}{\theta^2}\frac{2}{\beta}\frac{\Omega}{(e - \Omega)}\ln(e - \Omega)$ with $\Omega = (e-1)\left(\frac{\theta_0}{\theta}\right)^{\frac{1}{\beta}}$	β	$\theta_0 \approx \frac{a}{\beta^2 + b\beta + a}$ $a = 5.4204$ $b = 6.5342$

864

865 Table 2 – Conditions of the heating and cooling experiments for the glycerin / water
866 mixture and for the CMC solution: inlet temperatures, external temperatures and flow
867 rates

Experiment	T_{in} (°C)	T_e (°C)	Q (L/min)
H1	20	80	0.5 / 1.0 / 1.5 / 2.0
H2	30	80	0.5 / 1.0 / 1.5 / 2.0
H3	40	80	0.5 / 1.0 / 1.5 / 2.0
H4	50	80	0.5 / 1.0 / 1.5 / 2.0
C1	60	10	0.5 / 1.0 / 1.5 / 2.0
C2	70	10	0.5 / 1.0 / 1.5 / 2.0
C3	80	10	0.5 / 1.0 / 1.5 / 2.0
C4	90	10	0.5 / 1.0 / 1.5 / 2.0

868

869 Table 3 – Mesh independence study of the 2D axisymmetric model

Mesh	N° of axial points	N° of radial points	N° of elements
M1	100	20	2 000
M2	200	40	8 000
M3	300	60	18 000
M4	400	80	32 000
M5	500	100	50 000
M6	600	120	72 000
M7	700	140	98 000
M8	800	160	128 000
M9	900	180	162 000
M10	1 000	200	200 000

870

871 Table 4 – Sum of squared errors (SSE) between the adjusted RTD models and the
872 experimental data for the glycerin/water mixture and for the CMC solution

Model	SSE	
	Glycerin/water	CMC
m-laminar	3.2×10^{-2}	2.9×10^{-2}
y-laminar	1.0×10^{-2}	1.3×10^{-2}
Sinusoidal	3.3×10^{-2}	2.4×10^{-2}
Exponential	1.1×10^{-2}	1.4×10^{-2}

873

874 Table 5 – Outlet temperatures obtained in the heating and cooling experiments for the
875 CMC solution

Experiment	T_{out} (°C)	T_{out} (°C)	T_{out} (°C)	T_{out} (°C)
	0.5 L/min	1.0 L/min	1.5 L/min	2.0 L/min
H1	56.4	49.5	45.6	43.7
H2	63.8	59.5	54.5	52.2
H3	64.3	61.2	56.2	55.5
H4	67.1	63.1	61.6	59.7
C1	34.2	41.2	41.8	43.5
C2	36.8	48.4	51.6	55.8
C3	39.5	53.3	55.1	58.2
C4	42.7	54.4	59.5	62.5

876

877 Table 6 – Outlet temperatures obtained in the heating and cooling experiments for the
878 glycerin/water mixture

Experiment	T_{out} (°C)	T_{out} (°C)	T_{out} (°C)	T_{out} (°C)
	0.5 L/min	1.0 L/min	1.5 L/min	2.0 L/min
H1	61.6	53.3	45.9	42.5
H2	67.4	58.4	53.5	50.4
H3	68.1	61.2	57.9	55.8
H4	71.9	67.0	63.9	62.9
C1	31.6	38.0	41.1	43.1
C2	32.4	41.3	43.1	48.3
C3	33.5	47.0	49.9	52.3
C4	35.0	47.4	53.7	58.8

879

880 Table 7 – Viscosity, Reynolds number and Dean number ranges of the heating and cooling
881 experiments with the glycerin/water mixture for the flow rates of 0.5 to 2.0 L/min

Experiment	μ (mPa·s)	Re (-)	De (-)
H1	20.4 – 32.3	67 – 169	20 – 50
H2	14.5 – 21.0	93 – 259	28 – 76
H3	11.8 – 15.0	115 – 361	34 – 106
H4	9.19 – 10.7	146 – 502	43 – 148
C1	12.9– 16.3	83 – 420	25 – 124
C2	9.73 – 13.1	104 – 553	31 – 163
C3	7.69 – 10.6	127 – 697	37 – 205
C4	5.98 – 8.67	155 – 892	46 – 263

882

883 Table 8 – Viscosity, Reynolds number and Dean number ranges of the heating and cooling
884 experiments with the CMC solution for the flow rates of 0.5 to 2.0 L/min

Experiment	K (Pa·s^n)	n (-)	Re_g (-)	De (-)
H1	1.63 – 1.95	0.421 – 0.436	9 – 70	3 – 21
H2	1.27 – 1.49	0.444 – 0.460	10 – 79	3 – 23
H3	1.11 – 1.24	0.462 – 0.474	11 – 85	3 – 25
H4	0.94 – 1.03	0.481 – 0.492	12 – 91	3 – 27
C1	1.12 – 1.27	0.460 – 0.472	10 – 88	3 – 26
C2	0.84 – 1.07	0.478 – 0.506	11 – 96	3 – 28
C3	0.71 – 0.91	0.496 – 0.525	12 – 100	3 – 29
C4	0.61 – 0.78	0.515 – 0.546	12 – 102	4 – 30

885

886 Table 9 – Results of the mesh independence study for the CMC solution: outlet bulk
887 temperature, absolute errors of temperature and computational time

Mesh	CMC heating			CMC cooling		
	$T_{b,out}$ (K)	Abs. Error (K)	time (s)	$T_{b,out}$ (K)	Abs. Error (K)	time (s)
M1	322.64	-	0.58	312.75	-	0.75
M2	326.28	3.64	2.30	315.70	2.95	2.33
M3	327.41	1.12	5.25	316.60	0.91	4.88
M4	327.94	0.54	8.92	317.04	0.43	8.92
M5	328.25	0.31	14.36	317.29	0.25	14.19
M6	328.45	0.20	21.83	317.45	0.16	20.39
M7	328.59	0.14	29.22	317.56	0.11	30.00
M8	328.70	0.10	40.11	317.64	0.08	39.42
M9	328.78	0.08	52.23	317.71	0.06	51.42
M10	328.84	0.06	64.27	317.76	0.05	67.50

888